

# The WALOP-North Instrument I: Optical Design, Filter Design, Calibration

John A. Kypriotakis<sup>a,b\*</sup>, Siddharth Maharana<sup>c, d\*</sup>, Ramya M. Anche<sup>c,j</sup>, Chaitanya V. Rajarshi<sup>c</sup>, A. N. Ramaprakash<sup>c,a,e</sup>, Bhushan Joshi<sup>c</sup>, Artem Basyrov<sup>g</sup>, Dmitry Blinov<sup>a,b</sup>, Tuhin Ghosh<sup>h</sup>, Eirik Gjerl w<sup>g</sup>, Sebastian Kiehlmann<sup>a,b</sup>, Nikolaos Mandarakas<sup>a,b</sup>, Georgia V. Panopoulou<sup>f</sup>, Katerina Papadaki<sup>a,b</sup>, Vasiliki Pavlidou<sup>a,b</sup>, Timothy J. Pearson<sup>e</sup>, Vincent Pelgrims<sup>k</sup>, Stephen B. Potter<sup>d,i</sup>, Anthony C. S. Readhead<sup>e,l</sup>, Raphael Skalidis<sup>l</sup>, Konstantinos Tassis<sup>a,b</sup>

<sup>a</sup>Institute of Astrophysics, Foundation for Research and Technology-Hellas, Voutes, 70013 Heraklion, Greece

<sup>b</sup>Department of Physics, University of Crete, Voutes, 70013 Heraklion, Greece

<sup>c</sup>Inter-University Centre for Astronomy and Astrophysics, Post bag 4, Ganeshkhind, Pune, 411007, India

<sup>d</sup>South African Astronomical Observatory, PO Box 9, Observatory, 7935, Cape Town, South Africa

<sup>e</sup>Cahill Center for Astronomy and Astrophysics, California Institute of Technology, Pasadena, CA, 91125, USA

<sup>f</sup>Department of Space, Earth and Environment, Chalmers University of Technology, 412 93, Gothenburg, Sweden

<sup>g</sup>Institute of Theoretical Astrophysics, University of Oslo, P.O. Box 1029 Blindern, NO-0315 Oslo, Norway

<sup>h</sup>School of Physical Sciences, National Institute of Science Education and Research, HBNI, Jatni 752050, Odisha, India

<sup>i</sup>Department of Physics, University of Johannesburg, PO Box 524, Auckland Park 2006, South Africa

<sup>j</sup>Steward Observatory, University of Arizona, Tucson, Arizona, 85721, USA

<sup>k</sup>Universit  Libre de Bruxelles, Science Faculty CP230, B-1050 Brussels, Belgium

<sup>l</sup>Owens Valley Radio Observatory, California Institute of Technology, MC 249-17, Pasadena, CA 91125, USA

**Abstract.** The Wide Area Linear Optical Polarimeter North (WALOP-North) is an optical polarimeter designed for the needs of the PASIPHAE survey. It will be installed on the 1.3m telescope at the Skinakas Observatory in Crete, Greece. After commissioning, it will measure the polarization of millions of stars at high Galactic latitude, aiming to measure hundreds of stars per  $deg^2$ . The astronomical filter used in the instrument is a modified, polarimetrically-neutral broadband SDSS-r. This instrument will be pioneering one due to its large field-of-view (FoV) of  $30 \times 30 arcmin^2$  and high accuracy polarimetry measurements. The accuracy and sensitivity of the instrument in polarization fraction will be at the 0.1% and 0.05% level, respectively. Four separate  $4k \times 4k$  CCDs will be used as the instrument detectors, each imaging one of the 0 deg, 45 deg, 90 deg and 135 deg polarized FoV separately, therefore making the instrument a four-channel, one-shot polarimeter. Here, we present the overall optical design of the instrument, emphasizing on the aspects of the instrument that are different from WALOP-South. We also present a novel design of filters appropriate for polarimetry along with details on the management of the instrument size and its polarimetric calibration.

**Keywords:** polarimetry, optical polarimetry, PASIPHAE, WALOP, optics, wide field polarimeter.

\*J.A.K.: [ikyriot@physics.uoc.gr](mailto:ikyriot@physics.uoc.gr)

\*S.M.: [siddharth@sao.ac.za](mailto:siddharth@sao.ac.za)

## 1 Introduction

Our collaboration, PASIPHAE (Polar-Areas Stellar Imaging in Polarimetry High Accuracy Experiment),<sup>1</sup> aims to map the magnetic field permeating the Galaxy's dust clouds in three dimensions

40 by analyzing the polarization of stars. Starlight is usually not intrinsically polarized, but when  
41 there is interstellar dust aligned with the magnetic field in the path between the observer and the  
42 star, the light becomes polarized. The presence of this Galactic foreground hinders accurate mea-  
43 surements of the polarization of the Cosmic Microwave Background. By inferring the direction  
44 of the Galactic magnetic field in different interstellar clouds along the line of sight, using stars as  
45 probes, the PASIPHAE survey seeks to remedy that.<sup>1-3</sup> Wide field polarimeters with high mea-  
46 surement accuracy (up to 0.1% in polarization fraction) are needed to achieve this goal.<sup>1</sup> Two ded-  
47 icated instruments, Wide Area Liner Optical Polarimeters (WALOP-North and WALOP-South),  
48 are constructed in IUCAA, India. The survey will cover high latitude regions in both Galactic  
49 hemispheres after these two instruments are commissioned at the Skinakas Observatory in Greece  
50 (WALOP-North) and the SAAO Observatory in South Africa (WALOP-South), respectively. Of  
51 the two WALOP instruments, WALOP-South<sup>4-6</sup> was designed first and used as a reference to  
52 make the WALOP-North instrument. In this article, we discuss the optical design and calibration  
53 of WALOP-North, focusing on aspects of the design that are different from that of WALOP-South.  
54 Section 2 presents the technical requirements from the instrument design. Section 3 gives the  
55 details of the instrument design. Section 4 presents the instrument performance. Section 5 docu-  
56 ments the procedure of choosing the filters and designing ones appropriate for polarimetry. Finally,  
57 section 6 presents the polarimetric calibration strategy for the instrument.

## 58 **2 Technical Requirements**

59 Table 1 lists the technical specifications for the instrument that stem from PASIPHAE survey's  
60 scientific goals.<sup>1</sup> These choices were made after considering the materials and technology readily  
61 available, as well as the most recent advancements in polarimeter designs.

62 *2.1 Sensitivity and accuracy*

63 The science requirements demand that the device be able to obtain a  $5\sigma$  measurement (before bias  
 64 correction<sup>7,8</sup>) for  $p \geq 0.5\%$  and magnitude  $\leq 16.5$  in the sdss-r' band. In other words, the in-  
 65 strument's sensitivity ( $s$ ) and accuracy ( $a$ ) must be better than 0.05% and 0.1%, respectively. We  
 66 define  $s$  as the maximum systematic uncertainty and internal noise introduced by the instrument,  
 67 and  $a$  as the largest standard deviation (STD) of the measured polarization from the actual polar-  
 68 ization respectively (for a star of magnitude 16.5 and polarization fraction 0.5 with an exposure of  
 69 20 minutes).

70 The calculations mentioned above refer to the stars' ideal photometry. For it to be possible, the  
 71 instrument's imaging capabilities must be superior to (or at least on par with) the site's seeing.<sup>9</sup>  
 72 This means that the instrument must accurately sample the stars' point spread function (PSF) while  
 73 minimizing any PSF distortion or enlargement caused by air turbulence.

Minimum Polarimetric Sensitivity	0.05%
Minimum Polarimetric Accuracy	0.1%
FoV	$30 \times 30 \text{ arcmin}^2$
Shots per Measurement	1
Channels (# CCDs)	4
Imaging Performance	seeing limited PSF size (1.1arcsec FWHM)
CCD Size (px)	$4096 \times 4096$
Pixel Size	$15\mu\text{m} \times 15\mu\text{m}$
Main Optical Filter	SDSS-r
Stray&Ghost Light Level	Least possible, less than the Sky brightness
Size	Compatible with the Skinakas 1.3 m telescope

Table 1: Technical specifications for the WALOP-North Instrument.

## 74 2.2 Field of view and detectors

75 For the initial survey to be completed in 2 years, the instrument's field of view (FoV) must be  
76 around  $30' \times 30'$ , per the technical requirements and accuracy determined above. In addition, the  
77 CCDs must have 4096 pixels in each dimension, therefore sampling the sky with a plate-scale  
78 of  $0.43945 \frac{\text{arcsec}}{\text{px}}$ , in order to accurately sample the PSF (at least 2 pixels per full width at half  
79 maximum (FWHM) - Nyquist limit<sup>10,11</sup>) at Skinakas (mean seeing FWHM of 1.1"). In this setting,  
80 the instrument's plate scale decreases to 0.44" per pixel, enabling the PSF to occupy 2.3 pixels per  
81 fwhm. Experience has proven that one-shot polarimetry is preferable for achieving the accuracy  
82 and sensitivity requirements mentioned earlier, in the shortest amount of time possible. Such  
83 polarimeters, like RoboPol,<sup>12</sup> measure the Stokes parameters precisely and in a timely fashion. In  
84 this kind of polarimetry, images of the target are concurrently captured at polarization angles of 0,  
85 45, 90, and 135 degrees. The improved accuracy of 4-channel polarimeters comes from the fact  
86 that the signal is simultaneously acquired in all needed channels, therefore reducing what would  
87 be channel-to-channel variability (e.g. due to atmospheric effects on the channels throughput).  
88 These polarimeters do suffer from differential effects across the multiple beams and either had  
89 a narrow field of view or lower accuracy over a wider field<sup>13,14</sup> in an attempt to mitigate those  
90 differential effects. In our case, sacrificing either the FoV size or accuracy was unacceptable due  
91 to the survey's time constraints and the instrument's accuracy restrictions. As a result, we needed  
92 to use four different, yet extremely precise CCDs, each for imaging a different polarization angle  
93 from the ones mentioned above (four channels, one shot polarimetry).

94 2.3 Size of the instrument

95 The instrument will be mounted on the 1.3-meter telescope at the Skinakas observatory. The weight  
96 of the instrument must not be greater than roughly 200 kg in order not to exceed the torque limit  
97 of the telescope's motors. The instrument's size is another constraint because it must fit inside  
98 the telescope's mounting fork. In Figure 1, the fork clearance is displayed. The focal plane (FP)  
99 is separated from the top of the fork body by a distance of 473.8 mm, and from the back of the  
100 primary mirror cell by a distance of 526.2 mm. This permits an instrument to have a maximum  
101 length of 1000 mm, assuming that the optics will be positioned on the optical axis before the focal  
102 plane.

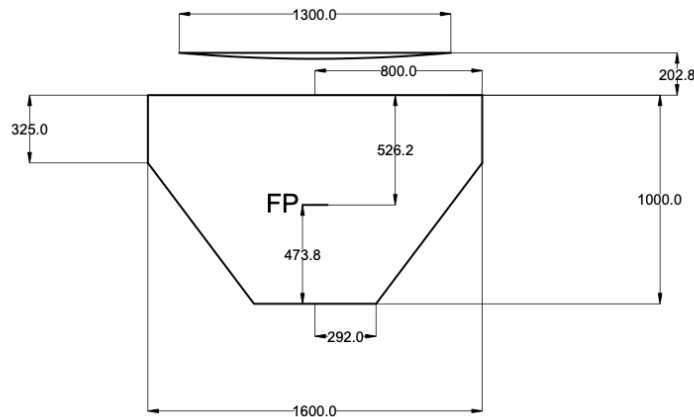


Fig 1: The clearance inside the fork of the Skinakas observatory's 1.3m telescope. All measurements are in mm. FP is the used telescope's focal plane, after the shift described in Section 3.1.

103 2.4 Filter

104 Ghost rays and stray light will affect such an instrument, by introducing extra background inten-  
105 sity and skewing the morphology of the image features. It is up to the design to reduce them to  
106 the brightness of the sky (or less), effectively eliminating their impact on the measurement. The  
107 instrument must function with the SDSS-r filter in place (Section 5). This necessitates that it be  
108 tuned for wavelengths in the 5000–7000Å range, while no polarization must be added by the filters  
109 utilized.

110 **3 Instrument Design**

111 This section will discuss the instrument design and the challenges encountered to attain the desired  
112 performance. The design concept of both WALOP-North and its counterpart WALOP-South is  
113 presented in Figure 2, while the annotated shaded model of the instrument is shown in Figure 3.

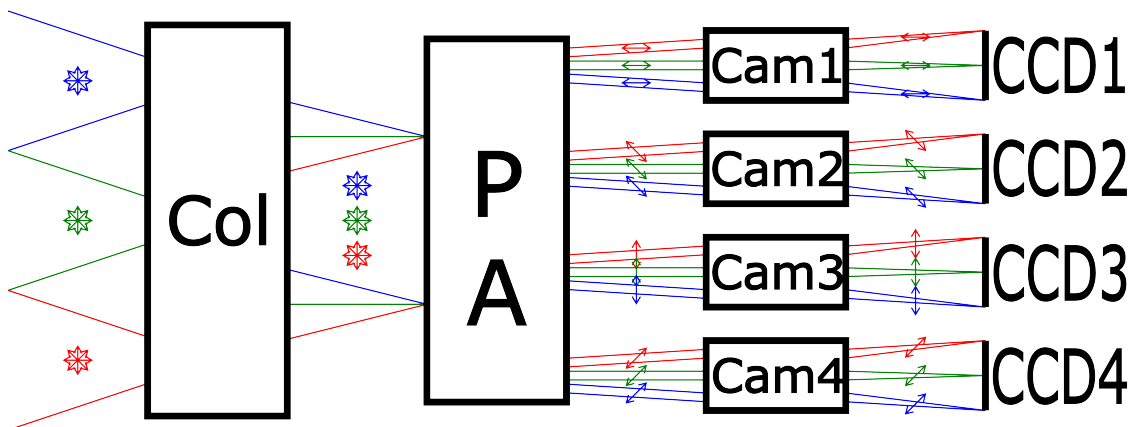


Fig 2: A conceptual diagram of the WALOP instruments. Light enters the collimator ("Col" - from the left, coming from the telescope). It is then fed to the polarization array ("PA" - containing 2 Wollaston prisms side-by-side each preceded by a HWP), whereby is split into 4 beams. The now polarized light is focused by 4 camera lens arrays ("Cam1-4") onto 4 separate CCDs. The diagram represents the WALOP-North instrument whose collimator receives unfocused light (as discussed in Section 3), while WALOP-South receives the light already focused by the telescope. The arrows denote the polarization of the rays.

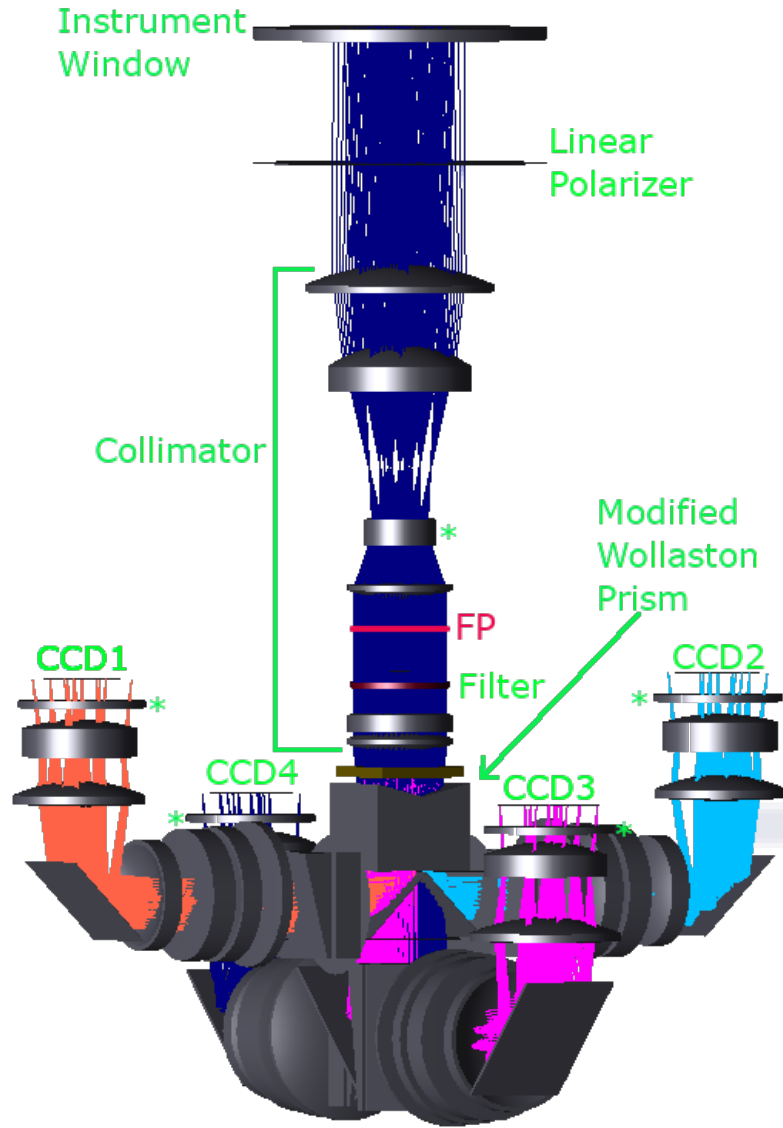


Fig 3: The shaded model of the instrument. Light coming from above passes through the collimator, enters the side-by-side Wollaston prisms (being split in 4 beams by polarization) and is re-directed horizontally to 4 separate camera arms. In each of those arms, a second fold redirects the light upwards towards a CCD. The linear polarizer is removable and rotatable, to be used for calibration (Section 6). Asterisks denote aspheric lenses. FP is the focal plane of the telescope (without the instrument optics) in the modified configuration of Section 3.1.

114 WALOP-North's optical design is similar to the WALOP-South instrument<sup>4-6</sup>, as identical  
 115 polarizer optics are used; the differences are in the design of the collimator and cameras. This  
 116 paper will concentrate on the key differences between the instruments listed below:

- 117 • Target Telescope

- 118 • Optics Placement
- 119 • Folding of the Beams
- 120 • Usage of Aspherical Optics
- 121 • Guider Design

122 Other minor differences between the two instruments include the placement of the filter be-  
123 tween collimator lenses (in the case of WALOP-North) and the size of the FoV that, in the case of  
124 WALOP-South, is increased to 35'x35'.

### 125 *3.1 Telescope and Site Details*

126 WALOP-North will operate at the 1.3m telescope at the Skinakas observatory. The instrument,  
127 which is directly affixed to the telescope's chassis structure, will take the place of the current  
128 GAM (Guiding and Acquisition Module).

129 In order to meet the size requirements for the instrument, we decided to shift the focal plane of  
130 the instrument upwards (closer to the primary mirror) by 119.8mm. In order to do this we have to  
131 move the secondary mirror from the nominal position by about 15mm. This shifted the f-number  
132 of the telescope from  $f/7.6$  to  $f/8$ . The shifted focus is not the nominal for the telescope, nor the  
133 optimal in terms of spot sizes produced at the new focal plane. The collimator lenses of WALOP-  
134 North correct the spot sizes (acting as pre-optics in addition to their collimating duty). This is a  
135 major difference from the WALOP-South design.

136 Table 2 lists some details of the telescope and observatory that will host the instrument. These  
137 were used in the design of WALOP-North to guide the process and check the instrument compati-  
138 bility and performance.



Telescope Type	Modified Ritchey-Chrétien
Primary Mirror Diameter	1290mm
Secondary Mirror Diameter	429mm
Telescope's Nominal f/#	7.6
Telescope's Used f/#	8
Plate Scale at the focal plane (FP)	$0.01991 \frac{\text{arcsec}}{\mu\text{m}}$
Plate Scale of instrument + telescope	$0.02930 \frac{\text{arcsec}}{\mu\text{m}}$
Pixel Size of the WALOP CCDs	$15\mu\text{m} \times 15\mu\text{m}$
Optical Axis Between FP and Chassis (upwards)	526.2mm
Optical Axis Between FP and Chassis (downwards)	473.8mm
Site Altitude (above Mean Sea Level)	1750m
Median Seeing of the Site	1.1"
Operational Temperature Range at the Site	$(-5 - 30)^{\circ}\text{C}$

Table 2: Telescope and Site Details for the Skinakas 1.3m telescope.

### 139 3.2 Optics Placement

140 In the case of WALOP-North, we had to place some of the collimator optics before the focal plane  
 141 of the telescope (pre-optics) due to size limitations. This enabled us to save space along the optical  
 142 (z-) axis of the instrument, therefore allowing us to match the constraints.

### 143 3.3 Folding of the Beams

144 Another strategy used in WALOP-North exclusively was folding the beams an additional time  
 145 within the camera optics, as seen in Figure 3. The camera fold happens towards the negative-z  
 146 direction to avoid reduction of transmittance due to Brewster-angle effects.<sup>15</sup> This was a necessity  
 147 since the size constraints along the  $x$  and  $y$  axes were not permitting of a larger instrument.

148 *3.4 Usage of Aspherics*

149 One of the instruments’ design goals was to minimize the usage of aspheric lenses in the design due  
150 to the complications arising from their utilization. One such complication is that aspheric lenses  
151 are much harder to manufacture, and therefore more expensive and perhaps unfeasible. Another  
152 hurdle in the integration of aspheric lenses is their proper alignment with the optical beam. Due to  
153 the space constraints in WALOP-North, this type of lens was not avoided completely, and one such  
154 lens exists in the collimator, in addition to one more aspheric lens in each camera arm. Details of  
155 said lenses are given in Table 3.

<b>Lens</b>	<b>ROC</b>	<b>Glass</b>	<b>t</b>	<b>D</b>	<b>k</b>
Collimator, Lens 3	-50/98	S-FPL53	10mm	53mm	0.253
Ordinary Cameras, Lens 6	-62/-171	H-QF50	15.8mm	90.4mm	-1.262
Extraordinary Cameras, Lens 6	-62/-171	H-QF50	15.8mm	90.4mm	-1.330

Table 3: Aspherical Lenses used in WALOP-North. ROC is the radius of curvature, D is the lens diameter, t is the thickness, and k is the conic parameter

156 *3.5 Guider Design*

157 WALOP-South<sup>5</sup> is using an off-axis-pickup guiding system that trails around the science field in  
158 a 2-axes XY stage. For WALOP-North, we designed a rotatory system, where the autoguider  
159 rotates around the science field. A comparison of the two design approaches is shown in Figure 4.  
160 Trailing has the advantage of the light-pickup being always as close to the science field as possible  
161 and always aligned to the science field. On the other hand, a rotating guider has the advantage of  
162 the light pickup being at a set distance to the optical axis at all times (therefore introducing less  
163 aberrations) and being able to perform a 360° rotation around it (that way increasing the available  
164 effective guider FoV).

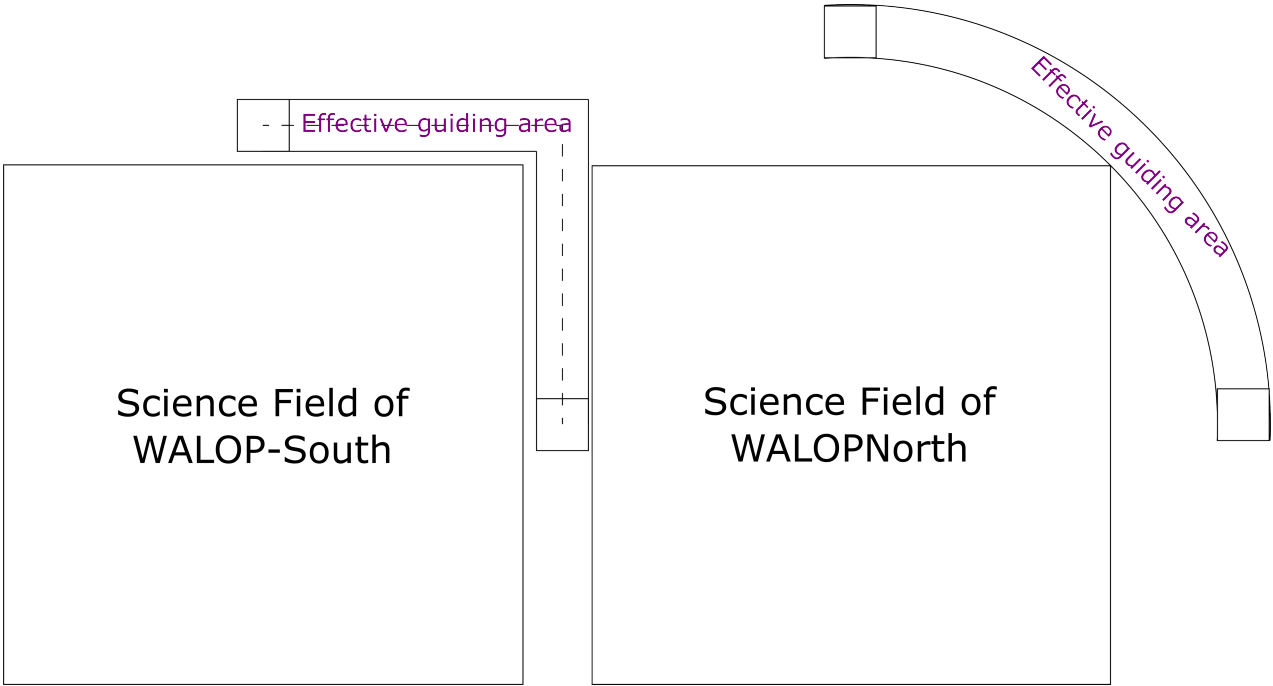


Fig 4: Comparison of a trailing guider concept, used in WALOP-South (left) and a rotating guider concept, used in WALOP-North (right). The small squares in each case are the guider fields and the big ones, the science fields in each case (the rotating design’s path has been truncated to 90° for illustration purposes).

165 **4 Instrument performance**

166 *4.1 PSF Morphology*

167 The first metric of the instrument performance is the PSF width and morphology. The Zemax-  
 168 generated, wavelength weight-averaged (according to the SDSS-r filter), FoV-averaged PSF of the  
 169 instrument for all 4 different detectors is shown in Figure 5. From this we can see a symmetrical  
 170 distribution of the instrument PSF, with slight zero-offset at each detector in pairs of 2. Note that  
 171 this does not take into account the seeing, whose effect will be more apparent in the results of  
 172 Section 4.2 .

173 In order to account for the seeing in the PSF, we created plots of the instrument PSF convolved  
 174 with the seeing PSF (used as kernel). We convolved the PSF of Figure 5 with a Gaussian kernel

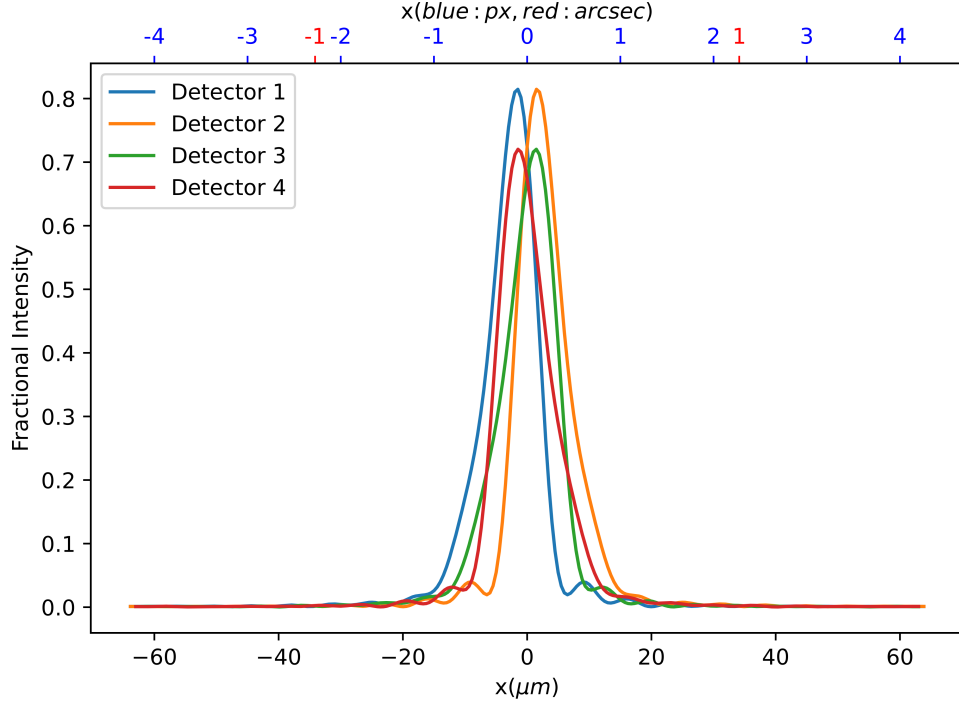


Fig 5: Plot of the PSF along the x-axis (in  $\mu\text{m}$ ,  $px$ , and  $\text{arcsec}$ ) for each instrument detector. Each PSF is weight-averaged for wavelength (using the SDSS-r bandpass) and averaged for the entire FoV. Seeing is not included in this calculation.

175 of  $FWHM = 1.1'' \Rightarrow \sigma = 0.4671''$  (producing Figure 6). The FWHM used is the expected  
 176 median at Skinakas (Table 2). Comparing Figure 6 with Figure 5 we conclude that our instrument  
 177 is indeed seeing-limited and that the PSF is accurately sampled as per the requirements<sup>1</sup>.

178 The PSF produced by the instrument is well within the requirements of the survey, as it is  
 179 accurately sampled and seeing-limited. The PSF is also symmetrical and well-behaved across the  
 180 entire field of view. Nevertheless small positioning errors are apparent in Figure 6. We intend  
 181 to deal with the differential nature of the PSFs using the instrument's dedicated image analysis  
 182 software (scope of a follow-up publication), following the data analysis pipeline of the RoboPol  
 183 instrument.<sup>16</sup>

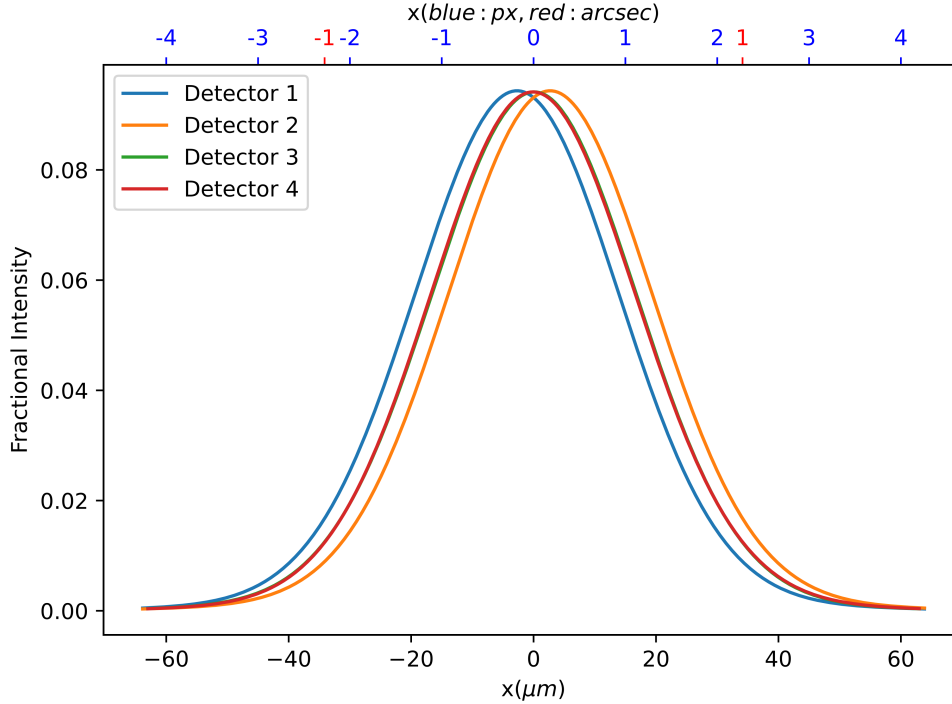


Fig 6: Plot of the PSF along the x-axis (in  $\mu m$ ,  $px$ , and  $arcsec$ ) for each instrument detector. Each PSF is weight-averaged for wavelength (using the SDSS-r bandpass) and averaged for the entire FoV. Seeing is included in this calculation, by means of convolving the seeing-ignorant PSF of Figure 5 with a Gaussian kernel of FWHM equal to the mean seeing FWHM at Skinakas.

#### 184 4.2 Encircled Energy Profiles

185 Another measure of the instrument performance is the encircled energy profiles, presented in Fig-  
 186 ure 7. The encircled energy profile of a spot on a detector gives us the energy detected within a  
 187 circle, centered at the spot centroid, of radius  $r$  with respect to  $r$ . These plots were created for the  
 188 spots produced on each detector, by a simulated star with a Gaussian seeing PSF and FWHM of  
 189 1.1'' (as per Section 2). We note that in all cases 99% of the incident light was recorded within  
 190 the Nyquist limit (Section 2) and the performance is seeing limited (comparing with the results of  
 191 Section 4.1).

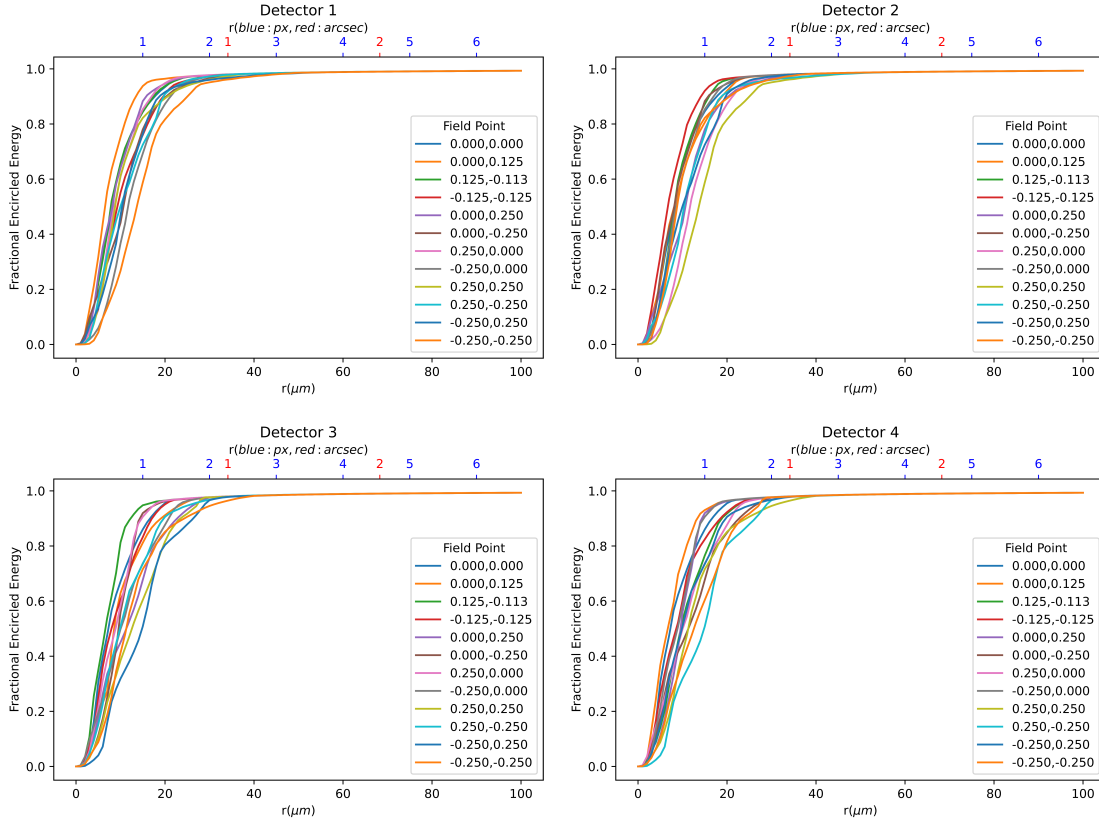


Fig 7: Encircled energy profiles for each detector and field position.

### 192 4.3 Spot profiles

193 The last metric we will use to assess the optical performance of our instrument is the spot sizes  
 194 and profiles at different field positions in all 4 detectors we used, presented in Figure 8. Most root-  
 195 mean-square (RMS) radii are below  $20\mu m$  (1.3px), while most geometric radii are below  $40\mu m$   
 196 (2.7px). We see that the entire field is well behaved and within the limits discussed in Section  
 197 2. Note that this calculation was done for a point-source object, similar to Section 4.1 (no seeing  
 198 effects included).

### 199 4.4 Tolerancing

200 The instrument performance was also evaluated under various tolerances, originating in misalign-  
 201 ments and manufacturing errors. The tolerancing criterion used was the RMS spot size, and the

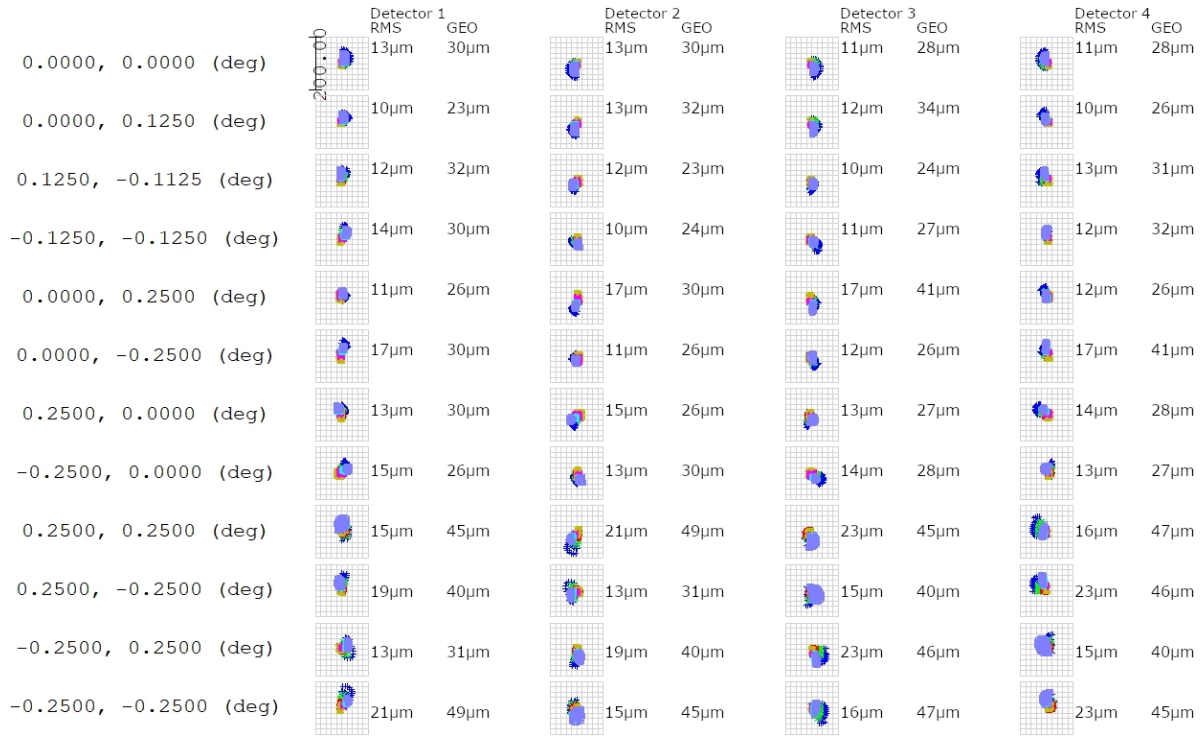


Fig 8: Spot diagram for the WALOP-North instrument. For every detector (columns) and field point (rows), the spot produced from 10000 simulated rays is depicted. Additionally, the RMS and Geometric radius (GEO) is mentioned next to the spot.

202 compensator was chosen as the back focus (distance between each CCD and the corresponding  
 203 final camera lens). The maximum compensation permitted was  $1mm$ . Table 4 lists the acceptable  
 204 tolerance values. A Monte Carlo tolerance analysis with compensation was performed for  $10^5$  test  
 205 systems. Table 5 lists the tolerancing results. We see that the criterion was kept below  $41\mu m$  in all  
 206 cases. The results show that the instrument is robust against the tolerances considered.

## 207 5 WALOP Filters

### 208 5.1 Choice of Filter

209 The SDSS-r filter has been selected for use with both WALOP instruments. Johnson-Cousins filters  
 210 have very broad profiles (compared to the SDSS ones). Given the wavelength-dependent dispersion  
 211 of birefringent optics, a wider filter would make the design substantially more difficult despite

<b>Parameter</b>	<b>Tolerancing Value</b>
Radii of Curvature	$\pm 100\mu m$
Thicknesses	$\pm 50\mu m$
Surface Decentering	$\pm 50\mu m$
Element Decentering	$\pm 30\mu m$
Surface Tilts	$\pm 1'$
Element Tilts	$\pm 2'$
Surface Irregularities	1.5 fringe at 633nm
Indices of Refraction	$\pm 0.0005$
Abbe Numbers	$\pm 0.5\%$

Table 4: Tolerancing parameters for the WALOP-North instrument.

<b>RMS Radius</b>	<b>Configurations 1&amp;2</b>	<b>Configurations 3&amp;4</b>
Nominal	$10.30\mu m$	$10.18\mu m$
Best	$10.43\mu m$	$10.44\mu m$
Worst	$40.88\mu m$	$36.04\mu m$
Mean	$17.87\mu m$	$17.45\mu m$
Standard Deviation	$3.58\mu m$	$3.29\mu m$

Table 5: Results of the Monte Carlo tolerance analysis for the WALOP-North instrument. The criterion used was the RMS spot size. The maximum compensation of the back focus was  $1mm$ .

212 being superior in terms of transmitted light. We determined the PSF-integrated photon flux for the  
 213 SDSS-r and Johnson-Cousins-R filters for a survey model star to securely exclude the Johnson-  
 214 Cousins-R filter. This was selected to be a SDSS-r  $16.5mag$  (cut-off magnitude for the survey),  
 215  $5180K$  (mean temperature of stars in PASIPHAE's intended area, according to the Besançon model  
 216 for stellar population synthesis of the Galaxy<sup>17</sup>) star. The PSFs used were those produced by Zemax  
 217 for the optimal instrument design for each filter.<sup>5</sup> At the Skinakas observatory, we also calculated  
 218 the value for the sky photon flux.<sup>9</sup> With those estimations, we could determine the mean (over  
 219 the entire field) photometric signal-to-noise ratio (SNR) for the instrument in either filter for a 20-



220 minute exposure. The results are reported in Table 6. Given its superior PSF characteristics and  
 221 apparent performance parity with the Johnson-Cousins-R filter, the SDSS-r filter was selected for  
 222 WALOPs.

	<b>Cousins-R</b>	<b>SDSS-r</b>
<b>Star Flux</b> ( $\frac{ph}{s \cdot cm^2}$ )	0.278	0.225
<b>Sky Flux</b> ( $\frac{ph}{s \cdot cm^2 \cdot arcsec^2}$ )	0.00779	0.00560
<b>SNR</b>	168	149

Table 6: Photometric Calculations for the WALOP candidate filters.

## 223 5.2 Making the filter non-polarizing

224 Glass substrates are covered with thin coatings to provide commercially available SDSS filters.  
 225 This impacts off-axis beam polarization in proportion to the incidence angle. The filter is posi-  
 226 tioned inside the collimator for WALOP-North, making it subject to beams with different inci-  
 227 dence angles. Therefore, we had to ensure that the filter we use would not cause the polarization  
 228 to increase past the instrument’s  $p = 0.1\%$  systematics goal. Given the transmittance curve of the  
 229 filter at various incidence angles, we can calculate the polarization introduced by the filter at any  
 230 incident angle for any incident polarization fraction. The highest polarization introduced by a com-  
 231 mercial SDSS-r filter (at a  $10^\circ$  angle of incidence (AOI), which is the extreme angle of incidence  
 232 on the WALOP filters, as per the design) was found to be above  $0.6\%$  (Figure 9). This does not  
 233 comply with the instrument’s limit; hence the creation of a modified SDSS-r filter was required.

234 We were able to design an SDSS-r filter with much lower induced polarization together with  
 235 Asahi Spectra Company.<sup>18</sup> The design of that filter consisted of fine-tuning the dielectric coatings  
 236 so that as low as possible polarization is introduced, while retaining a profile as similar as possible

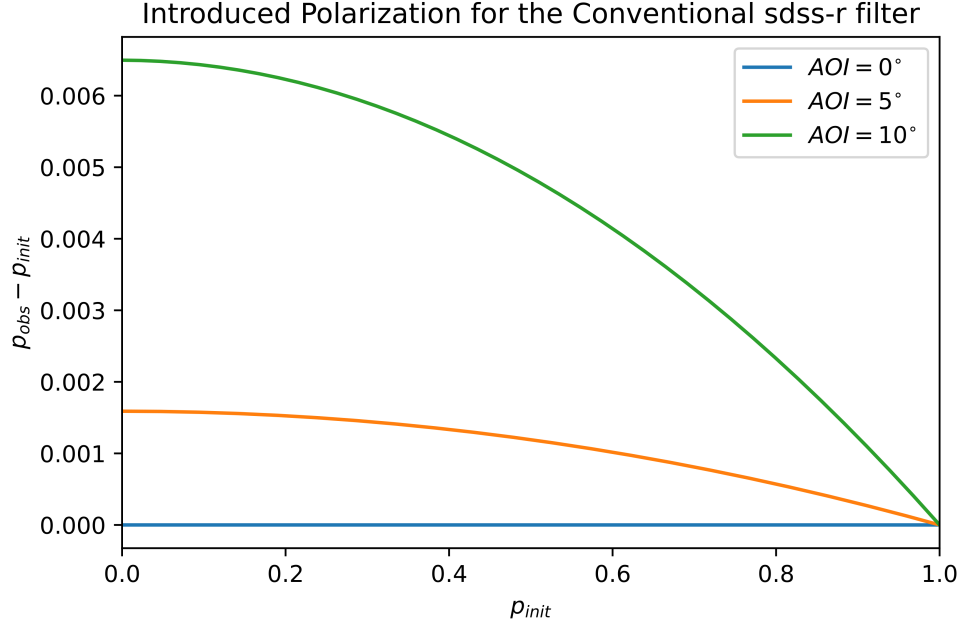


Fig 9: The polarization introduced by the conventional SDSS-r filter in different AOI as a function of the input polarization.  $p_{init}$  is the incident polarization to the filter and  $p_{obs}$  is the observed polarization after the filter (by an ideal polarimeter).

237 to the original SDSS-r. Figures 10 and 11 demonstrate its transmittance curve (which is identical  
 238 to the usual SDSS-r filter) and added polarization respectively.

### 239 5.3 Manufactured Filters

240 For our filters additional requirements must be met, since they have to perform optically in addition  
 241 to their spectral performance. They must not distort the image or have any optical power, like a  
 242 lens would. For the needs of the PASIPHAE project, 3 such filters were commissioned to Asahi  
 243 Spectra. One for each instrument (hereby filters A1 and A2) and a backup filter (hereby filter  
 244 B1). Appendix A shows the performance of these filters after manufacture. A summary of the  
 245 interferometry and spectroscopy results is presented in Table 7. We see that filters A1 and A2 are  
 246 very similar and up to par with the instrument requirements. Filter B1 is performing a bit worse,  
 247 yet also within the required limits for the instrument.

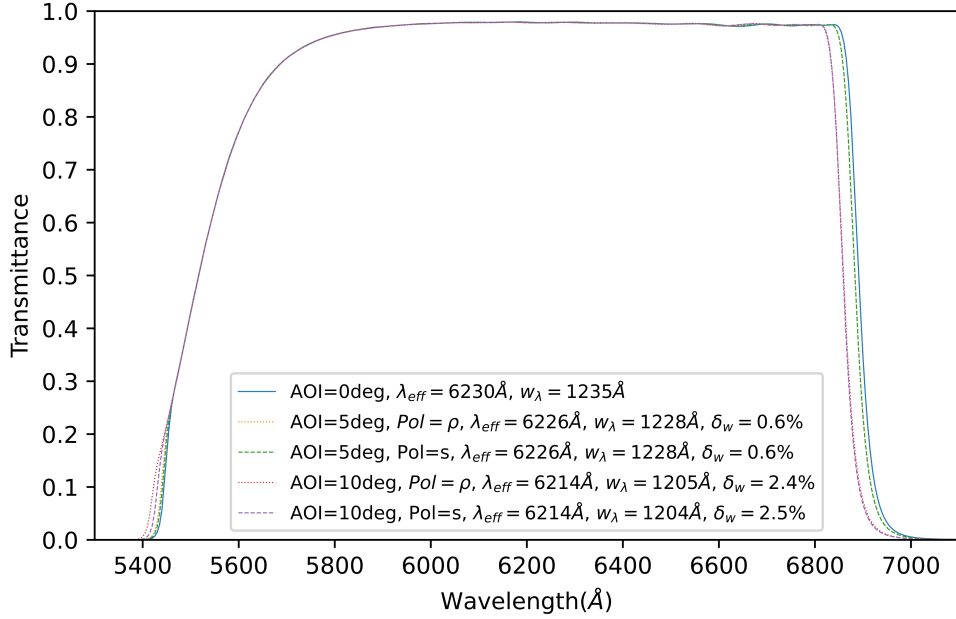


Fig 10: The transmittance curve of the new non-polarizing SDSS-r filter in two perpendicular polarization states ( $\rho$  and  $s$ ) and angles of incidence (lines intentionally thin to help distinguish the graphs).  $\lambda_{eff}$  is the effective wavelength of the filter,  $w_\lambda$  is the filter wavelength-width, and  $\delta_w$  is the wavelength-width difference between each respective  $AOI$  and  $AOI = 0^\circ$ . Note: we chose the nomenclature " $\rho$ " and " $s$ " for the filter's perpendicular polarization states instead of the conventional " $o$ " and " $e$ " to reflect the difference of reference frame between the filter and Wollaston prism (since both these components have a separate polarization angle reference frame). The reference frame of the Wollaston prism corresponds with the EVPA reference frame.

Filter	Max Optical Power	Max RMS Wavefront	$\max(p_{obs} - p_{init})$
<b>A1</b>	0.114 waves	0.0035 waves	0.025%
<b>A2</b>	0.077 waves	0.026 waves	0.025%
<b>B1</b>	0.128 waves	0.038 waves	0.030%

Table 7: Interferometric and spectroscopic performance of the manufactured WALOP filters.

## 248 6 Polarimetric Calibration

249 In order to calibrate the instrument, we will follow a similar methodology as prescribed for WALOP-  
250 South.<sup>6,19</sup> This is a numerical approach and not an analytical Stokes-Mueller<sup>20</sup> one, due to the  
251 instrument complexity. The following sections present the methodology we applied for the cali-

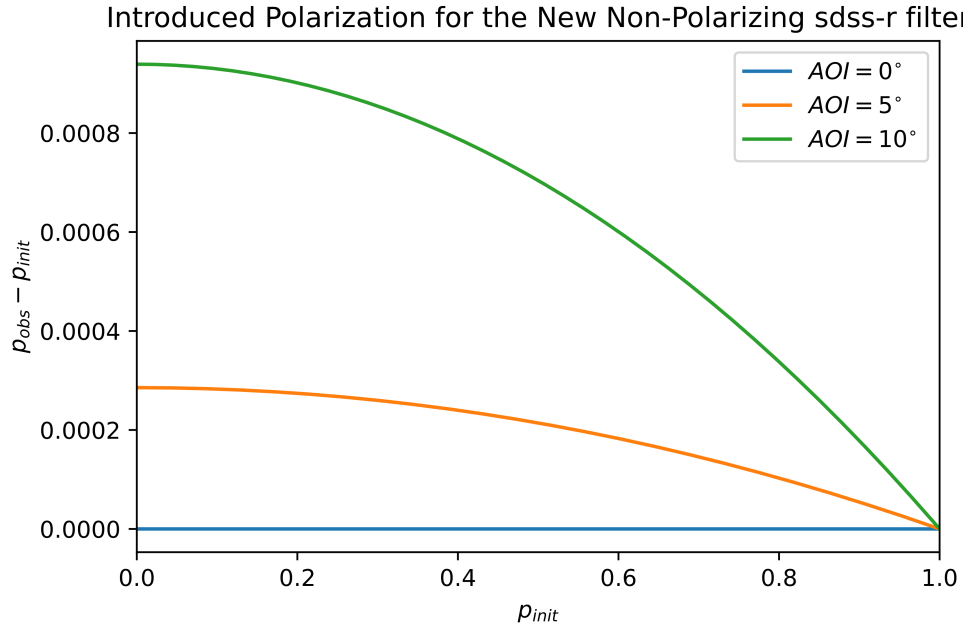


Fig 11: The polarization introduced by the new non-polarizing SDSS-r filter in different angles of incidence as a function of the input polarization.

252 bration of WALOP-North.

### 253 6.1 Zemax Simulations

254 Zemax OpticStudio provides the tools to simulate the system's (instrument+telescope) perfor-  
 255 mance. We can use OpticStudio<sup>1</sup> to calculate the output intensity in one of the 4 CCD detectors,  
 256 as a function of input intensity in a specific set of 12 field points per iteration. The drawbacks of  
 257 simulating the instrument using OpticStudio are the following:

- 258 • Each iteration will provide information on the output light intensity for 1 detector
- 259 • A limited number of field points (12) are available per iteration
- 260 • The light of the input beam is limited to being either unpolarized or fully polarized at a set  
 261 polarization angle

---

<sup>1</sup>in our case version 13

262 In order to overcome those limitations, we ran multiple sequential simulations each on different  
263 polarization state, field points and detectors. In the end, we combined the data from all detectors  
264 and field points, and interpolated the data from different polarizations (as shown in section 6.3)  
265 to extract the calibration of our instrument. That way, we can gain information for polarization  
266 states between 0 and 100% polarized, as well as infer the calibration for all field points between  
267 the limited amount simulated.

## 268 6.2 Zemax Inputs

269 The first step to running our tests was to generate the inputs for Zemax. We created the Zemax  
270 input files, containing the spatial coordinates of the field points sampling the entire FoV, and the  
271 polarization states simulated for every field position (all either 100% or 0% polarized). Then,  
272 we compiled a ZPL (Zemax Programming Language) script that took care of recursively feeding  
273 all the polarization and field coordinates to Zemax and producing Transmittance files for each  
274 detector. These files give us the total instrument transmittance at different wavelengths (within the  
275 SDSS-r' band, with effective wavelength dictated by the model star and the filter's band-pass) for  
276 each combination of detectors (4 total), field points (576 total - 1.25' sampling of the entire FoV)  
277 and polarization (50 total - 49 polarized states and 1 unpolarized) provided. We therefore ran a  
278 total of 115200 simulations, each of  $10^9$  rays. Figure 12 depicts the FoV sampling and Figure 13  
279 depicts the polarization sampling of the simulations.

## 280 6.3 Calibration Equations

281 We have now acquired the transmittance at each detector ( $D$  ranging from 1 to 4: integer), each  
282 field point ( $x, y$  ranging from -0.25 to 0.25 degrees) and each input fully polarized (or unpolarized)

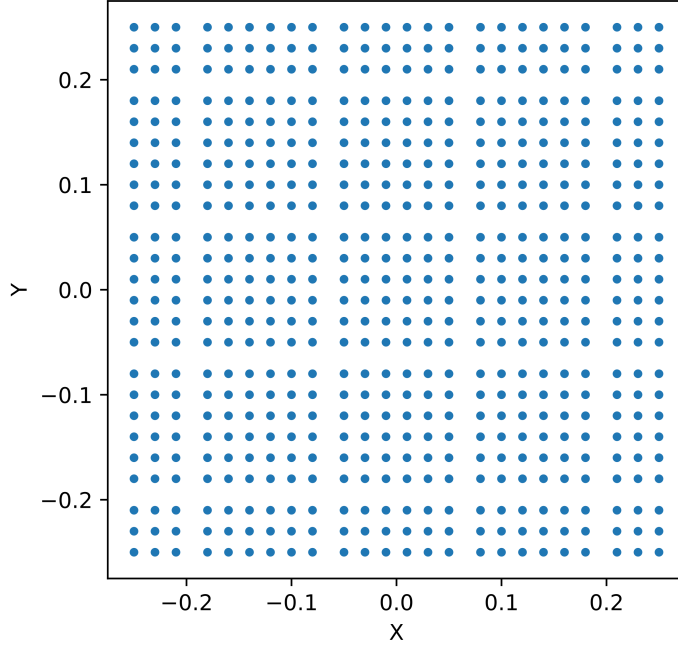


Fig 12: The FoV sampling we input to Zemax. (units of field are degrees)

283 state  $(q, u)$  ranging  $-1$  to  $1$  such that  $\sqrt{q^2 + u^2} = 0$  or  $1$ ). We shall name this transmittance  $T_{D,x,y,q,u}$ .

284 We denote the collection of all measured transmittances with a common parameter by replacing this

285 parameter with '\*' (grouping all consecutive \*s), e.g. the collection of all measured transmittances

286 of detector 2, will be named  $T_{2,*}$ , while all measured transmittances of detector 2, at the center

287 point will be  $T_{2,0,0,*}$ .

288 We denote  $q_r, u_r$  the input normalized Stokes parameters to the Zemax simulation. We define

289 as  $q_o, u_o$  the normalized Stokes parameters as observed by the uncalibrated instrument. For every

290 field point and every input polarization, the observed parameters are calculated as:

$$q_o = \frac{T_{3,*} - T_{1,*}}{T_{3,*} + T_{1,*}} \quad (1)$$

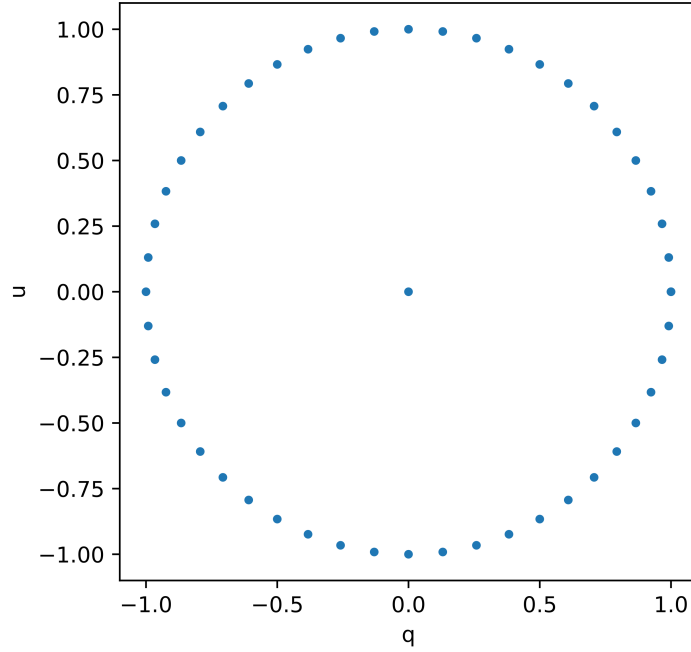


Fig 13: The polarization sampling we input to Zemax.

291

$$u_o = \frac{T_{2,*} - T_{4,*}}{T_{2,*} + T_{4,*}} \quad (2)$$

292

293

294

295

296

297

These differ from  $q_r$  and  $u_r$ , due to various instrument systematics caused by the dependence of polarization behavior of optical components on factors like angle of incidence and propagation of the beam, wavelength, birefringence variation across the beam etc.<sup>5,6,19</sup> As it is impractical to analytically model the combined effect of all this from first principles, we fit the input  $q$  and  $u$  parameters as second degree polynomials of  $q_o$  and  $u_o$  (using the Levenberg-Marquardt algorithm<sup>21,22</sup> through Scipy<sup>23</sup>):

298

$$q_r = a_0 + a_q q_o + a_u u_o + a_{q^2} q_o^2 + a_{u^2} u_o^2 + a_{qu} q_o u_o \quad (3)$$

$$u_r = b_0 + b_q q_o + b_u u_o + b_{q^2} q_o^2 + b_{u^2} u_o^2 + b_{qu} q_o u_o \quad (4)$$

299 The goal is to recover the coefficients  $a$  and  $b$  that will allow the mapping of the observed  
300 Stokes parameters to the input ones. To this model fitting, we add a 0.1% noise (by sampling  
301  $q_o$  and  $u_o$  from a Gaussian with 0.1% spread), as this is the level of expected noise to be faced  
302 during on-sky calibration. In contrast to WALOP-South's calibration,<sup>6</sup> the mixed term ( $qu$ ) has  
303 been added to the model. This is to reduce the fit's covariance.

#### 304 6.4 Verification of Calibration

305 In order to verify statistically our calibration, we need to be able to feed the model with mock  
306 observed data and compare the modeled against the theoretical instrument input  $q_i$  and  $u_i$ . Further-  
307 more, the instrument input needs to be partially polarized, much like the real cases the instrument  
308 will face.

309 To create this mock data, we first fit the transmittances discussed in Section 6.3 as second  
310 degree polynomials of  $q_r$  and  $u_r$ :

$$T_{1,*,q_r,u_r} = a_{1,0}^T + a_{1,q}^T q_r + a_{1,u}^T u_r + a_{1,q^2}^T q_r^2 + a_{1,u^2}^T u_r^2 + a_{1,qu}^T q_r u_r \quad (5)$$

311

$$T_{2,*,q_r,u_r} = a_{2,0}^T + a_{2,q}^T q_r + a_{2,u}^T u_r + a_{2,q^2}^T q_r^2 + a_{2,u^2}^T u_r^2 + a_{2,qu}^T q_r u_r \quad (6)$$

312

$$T_{3,*,q_r,u_r} = a_{3,0}^T + a_{3,q}^T q_r + a_{3,u}^T u_r + a_{3,q^2}^T q_r^2 + a_{3,u^2}^T u_r^2 + a_{3,qu}^T q_r u_r \quad (7)$$

313

$$T_{4,*,q_r,u_r} = a_{4,0}^T + a_{4,q}^T q_r + a_{4,u}^T u_r + a_{4,q^2}^T q_r^2 + a_{4,u^2}^T u_r^2 + a_{4,qu}^T q_r u_r \quad (8)$$

314 We then generate a mock set of  $q_i$  and  $u_i$ , sampling the entire Stokes plane (including partial  
315 polarization states that could not be included in the set of  $q_r, u_r$ ). We feed these parameters  
316 to the transmittance model (Equations 5-8), in place of  $q_r$  and  $u_r$ , generating a set of modeled



317 transmittances:  $T_{1,*}^m - T_{4,*}^m$ . From them, we calculate the mock observed  $q$  and  $u$  ( $q_o^m$  and  $u_o^m$ ), based  
318 on Equations 1 and 2, replacing  $T_{1,*} - T_{4,*}$ . These are then fed into the model (Equations 3 and 4),  
319 replacing  $q_o$  and  $u_o$  to produce the calibrated polarization ( $q_c$  and  $u_c$ ), which is then compared to  
320 the mock input polarization ( $q_i$  and  $u_i$ ).

## 321 6.5 Calibration Results

322 The first measure we used to evaluate our calibration model, is the covariance of the fit of Equations  
323 3 and 4, created by the fit itself described in Section 6.3. The covariance matrix is presented in  
324 Figure 14. From that, we understand that the fit is very well behaved, as no large covariance  
325 exists over the entire FoV. Some spots near the top right corner have a slightly larger covariance,  
326 especially in their  $qu$  term. This hints to a higher instrumental cross-talk in this region (discussed  
327 later in this Section). The non-vanishing covariance presented is the reason we chose to transition  
328 to a model that includes the  $qu$  term, as opposed to the calibration strategy of WALOP-South.<sup>6</sup>

329 The second metric of the success of the calibration is the standard deviation of the difference  
330 between the input ( $q_i, u_i$ ) and the retrieved ( $q_c, u_c$ ) parameters, for varying degrees of input polar-  
331 ization as described in Section 6.4. This is depicted in Figure 15. From that, we understand that the  
332 retrieved parameters adhere well to the inputs and therefore the instrument can be calibrated using  
333 the described strategy. There is a problematic area over an arc between the top and right edge of  
334 the FoV. This region's problematic behaviour is due to the large cross-talk between  $u$  and  $q$  at the  
335 half-wave plate (HWP) of the instrument's polarizing assembly at this region.

336 The final measure we use are the maps of the retrieved parameters for the following 2 fully  
337 polarized input parameters:  $(q_i, u_i) = (1, 0)$  and  $(0, 1)$ . These are depicted in Figure 16. The maps  
338 of  $q_c$  and  $u_c$  for  $(q_i, u_i) = (1, 0)$  and  $(q_i, u_i) = (0, 1)$  respectively are essentially the instrument's

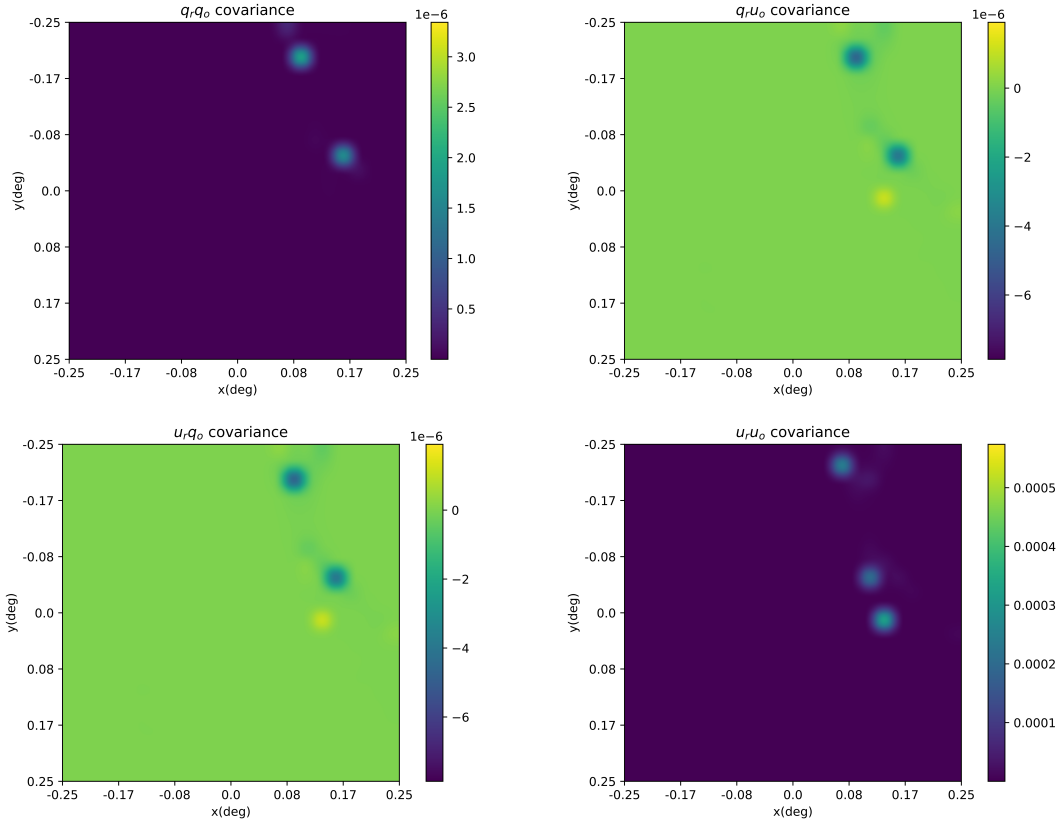


Fig 14: Maps of the elements of the covariance matrix from the fit on Equations 3 and 4.

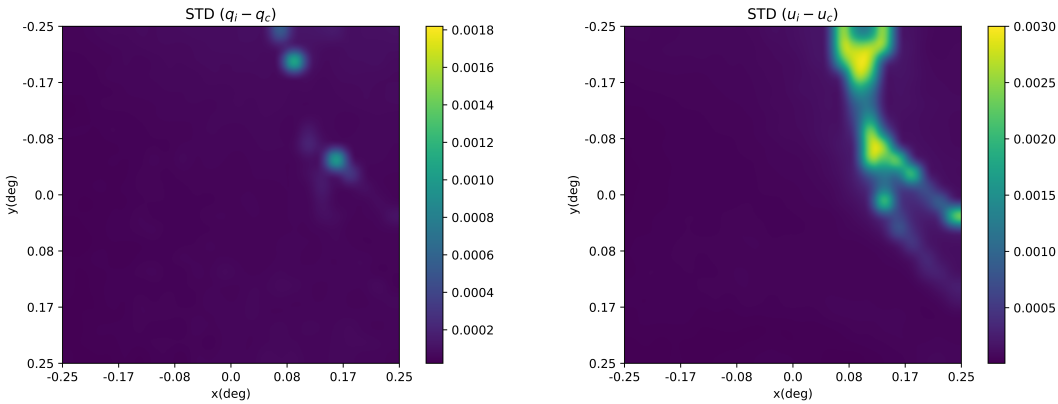


Fig 15: Maps of the standard deviations of the difference between the input and the retrieved  $q$  and  $u$  ( $a$  and  $b$  respectively) from the calibration model. The closer to 0, the better.

339 throughput (the amount of polarization in a specified Stokes parameter that gets recorded by the  
 340 instrument, without interference from the other parameter). The maps of  $q_c$  and  $u_c$  for  $(q_i, u_i) =$   
 341  $(0, 1)$  and  $(q_i, u_i) = (1, 0)$  respectively are essentially the instrument's cross-talk (the amount of  
 342 polarization in a specified Stokes parameter that gets recorded by the instrument, only as result of

343 the other parameter's value). From that, we understand that indeed the problematic areas in the  
 344 calibration are due to very high crosstalk at the region in the shape of an arc between the top and  
 345 right edge of the FoV. This is similar to the result for WALOP-South,<sup>6</sup> which utilizes the same  
 346 Wollaston prism assembly as the currently discussed instrument.

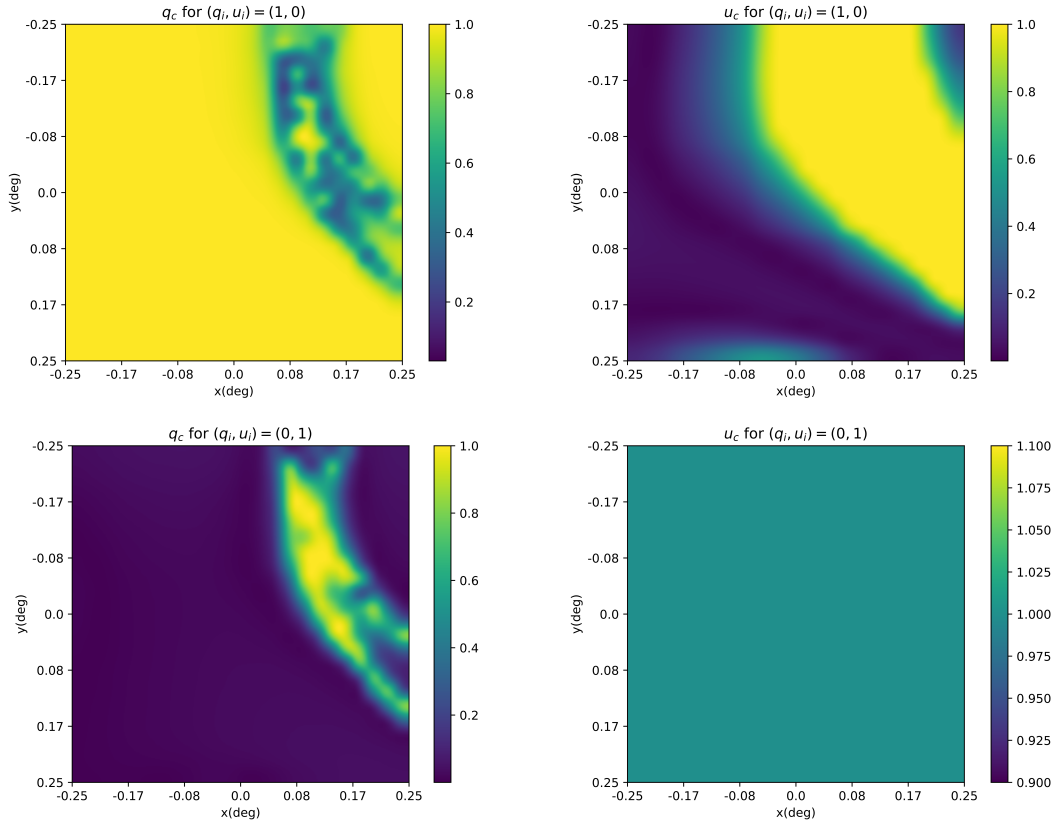


Fig 16: Maps of the retrieved parameters for the 4 polar fully polarized input parameters. Maps (a) and (d) depict the throughput of the instrument, while (b) and (c) the cross-talk.

### 347 6.6 On-Sky Calibration

348 After commissioning, the instrument will be able to follow the same polarimetric calibration pro-  
 349 cedure (as will WALOP-South<sup>6</sup>), using a polarizer mounted at the instrument entrance, before all  
 350 other optics.

351 This polarizer will be able to convert light from a dense stellar field (which sufficiently sam-

352 ples the FoV), irrespective of the polarization of stars, to fully-polarized. In conjunction with the  
353 polarizer's rotation, this creates a set of fully polarized inputs at any Electric Vector Polarization  
354 Angle (EVPA).

355 These observations, combined with observations of stars with known polarization<sup>24</sup> and of po-  
356 larimetric flat field sources such as the bright sky around near full-Moon creates a collection of  
357 observations of input sources with various polarizations. As part of developing the calibration pro-  
358 tocol for WALOP-South, we have shown that the sky around the Full Moon within a range of two  
359 days can serve as a highly effective polarimetric flat source (with an accuracy greater than 0.05%  
360 in p) for wide-field polarimeter calibration.<sup>25</sup> While the polarimetric sky flats allow for relative  
361 calibration of the full FoV, observing standard stars across the FoV allows absolute calibration for  
362 the full FoV.

363 Following the paradigm described in the current Section, we will be able to calibrate the instru-  
364 ment within the 0.1%*STD* instrumental level required, as shown in Figure 15. Furthermore, we  
365 have verified this calibration methodolgy in a lab-prototype of WALOP with accuracies matching  
366 the calibration model prediction.<sup>6</sup>

## 367 **7 Conclusion**

368 We have presented the optical design of WALOP-North, a wide-field linear optical polarimeter  
369 with a field of view  $0.25 \times 0.25 \text{ deg}^2$ , capable of reaching measured polarization accuracy of 0.1%.  
370 The polarimeter will be used by the PASIPHAЕ collaboration to carry out a polarimetric survey  
371 of the Galaxy. The instrument had design challenges, as it is intended to fit challenging spatial,  
372 polarimetric, and imaging constrains, which we have shown it is up to par with.

373 We showed a new design for filters that adhere to the SDSS-r standard, while introducing

374 minimal polarization to the wide field. The optical performance of the filters is also acceptable,  
375 since they introduce no significant aberration to the wavefront. Their design and testing methods  
376 we developed are extensible to other filters, as necessary for the polarimetric needs of WALOP-  
377 North and other polarimeters.

378 We also detailed a calibration strategy that accomplishes the strict requirements of the instru-  
379 ment performance, with minimal instrumental polarization in the end-result. We calibrate the pre-  
380 dicted instrument data to the desired accuracy. The procedure is suitable for on sky calibration of  
381 the instrument. Finally, the procedure is also applicable to the general-case scenario of calibrating  
382 large-FoV polarimeters.

## 383 **Appendix A: Manufactured Filter Performance**

### 384 *A.1 A1 Filter*

385 The transmittance curve and introduced polarization of the A1 filter are shown in Figures 17 and  
386 18 respectively.

387 The optical interferometry<sup>26</sup> at 3 different locations and wavefront measurement of the A1 filter  
388 are shown in Figures 19, 20 and 21.

### 389 *A.2 A2 Filter*

390 The transmittance curve and introduced polarization of the A2 filter are shown in Figures 22 and  
391 23 respectively.

392 The 3-level interferometry and wavefront measurement of the A2 filter is shown in Figures 24,  
393 25 and 26.

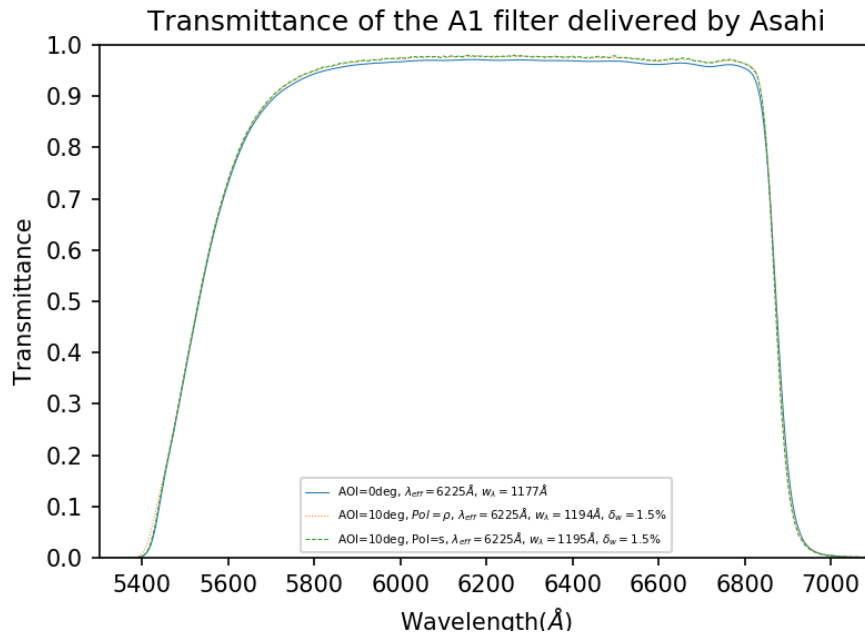


Fig 17: The transmittance curve of the A1 filter in different polarization states and 2 different angles of incidence.

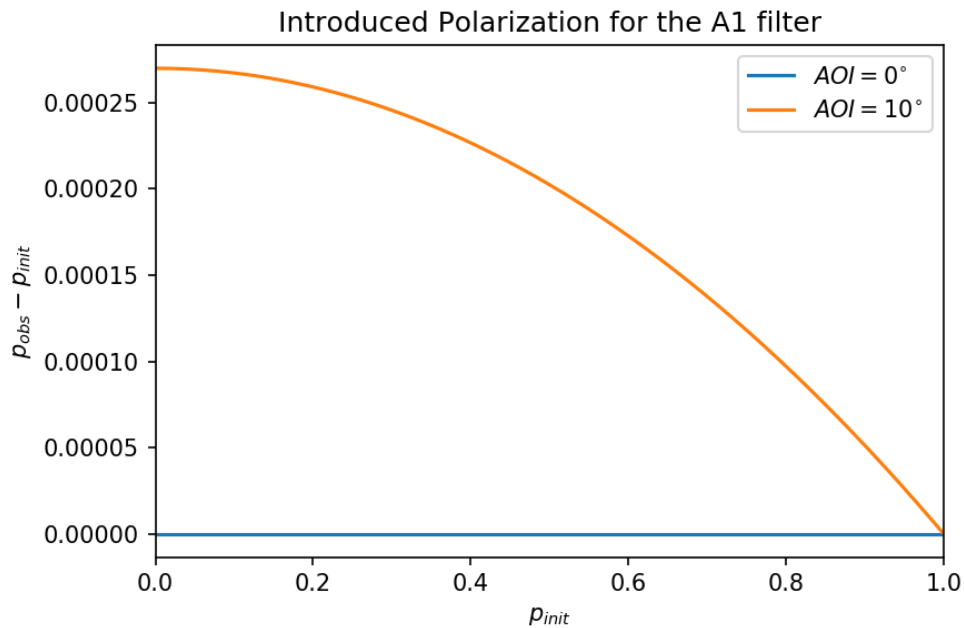


Fig 18: The polarization introduced by the A1 filter in 2 different angles of incidence (normal and extreme) as a function of the input polarization.

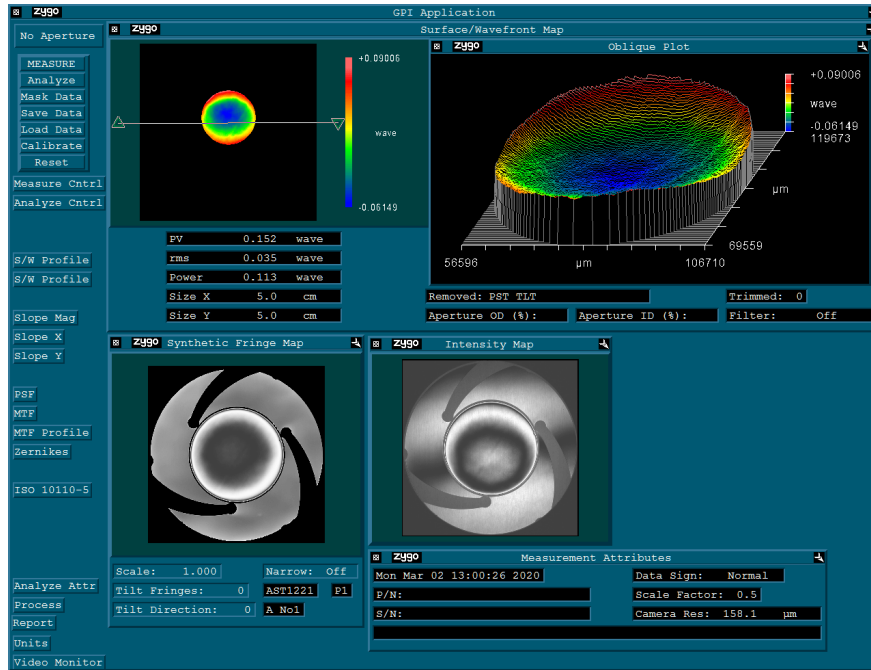


Fig 19: The first interferometric and wavefront measurement of the A1 filter.

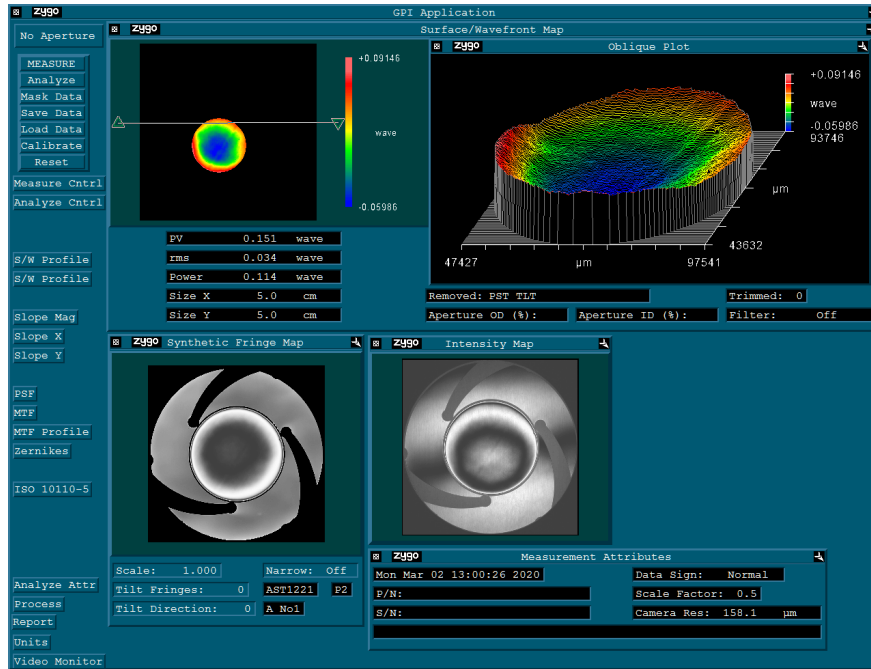


Fig 20: The second interferometric and wavefront measurement of the A1 filter.

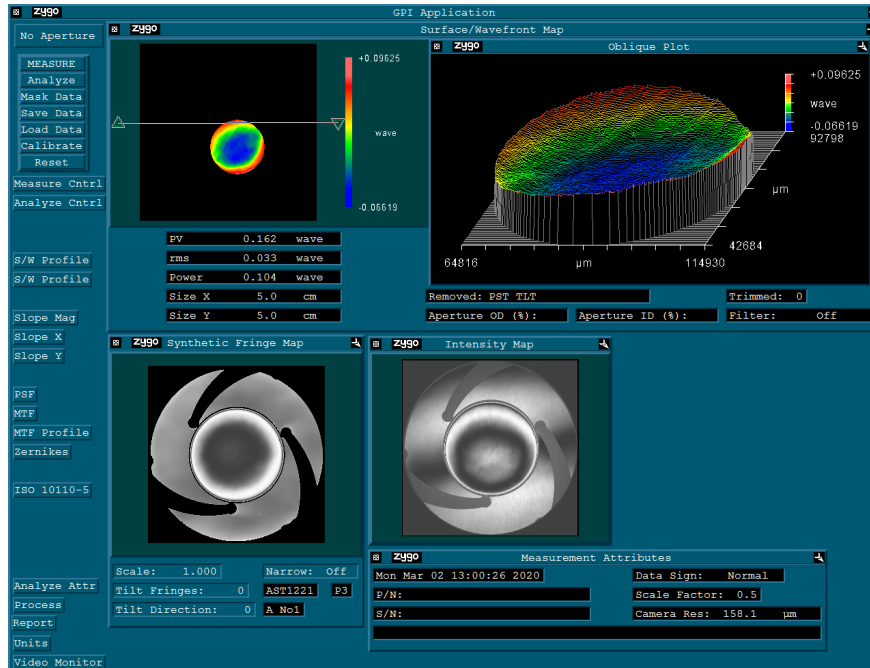


Fig 21: The third interferometric and wavefront measurement of the A1 filter.

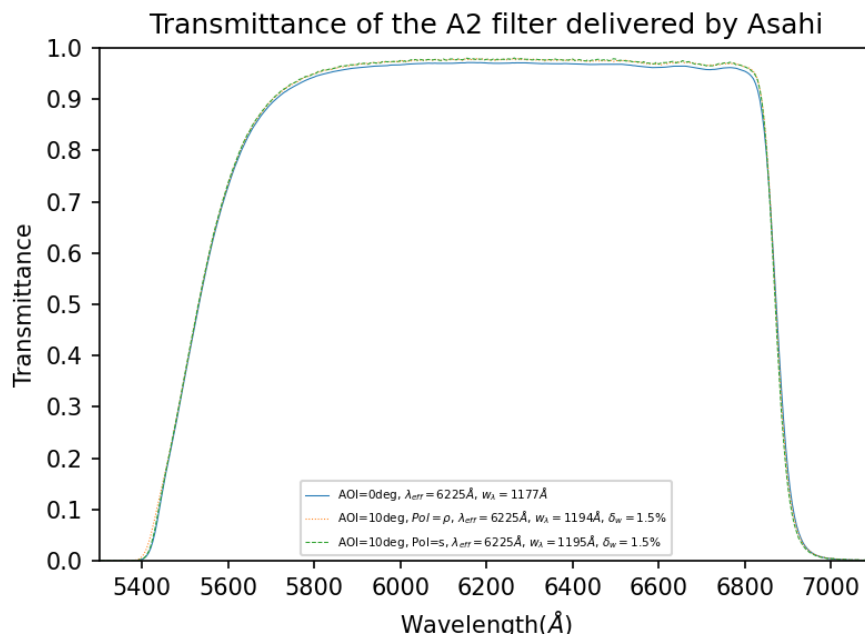


Fig 22: The transmittance curve of the A2 filter in different polarization states and 2 different angles of incidence.



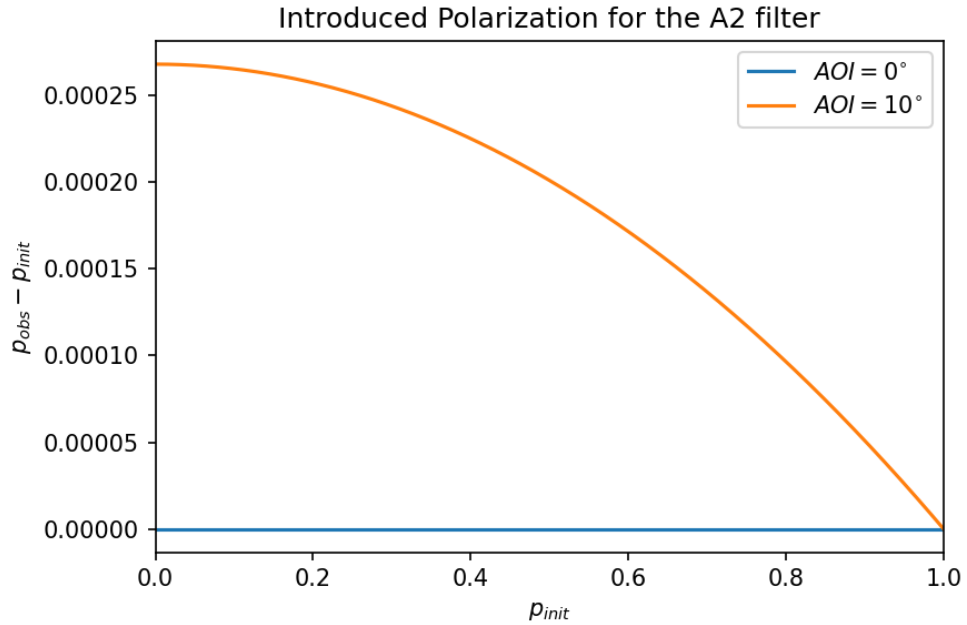


Fig 23: The polarization introduced by the A2 filter in 2 different angles of incidence (normal and extreme) as a function of the input polarization.

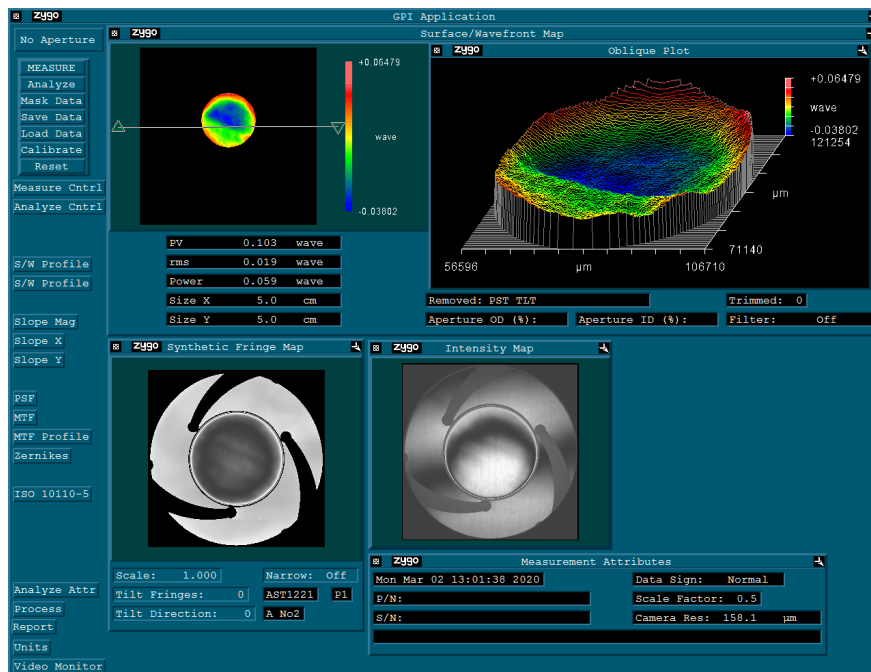


Fig 24: The first interferometric and wavefront measurement of the A2 filter.

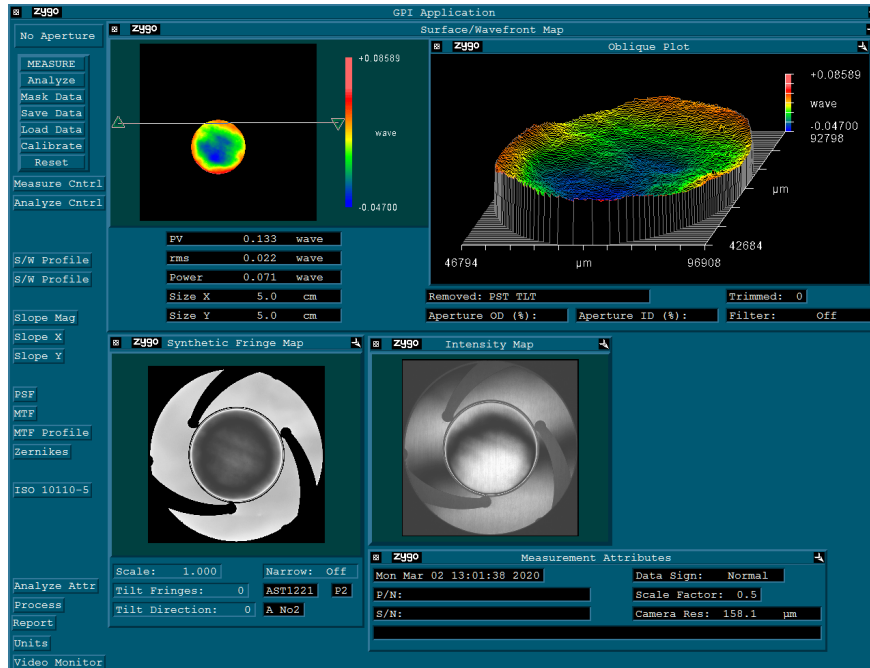


Fig 25: The second interferometric and wavefront measurement of the A2 filter.

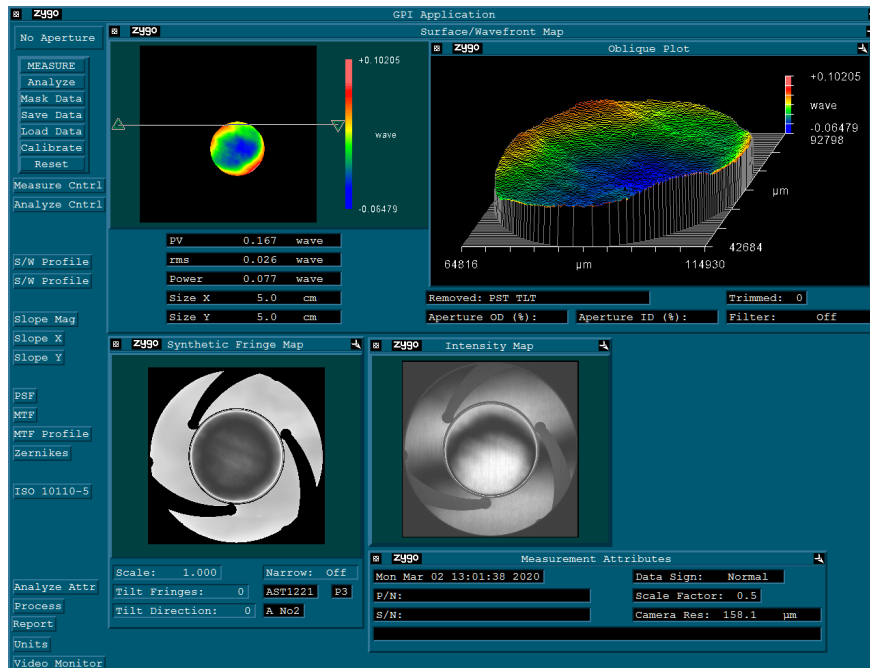


Fig 26: The third interferometric and wavefront measurement of the A2 filter.

394 *A.3 B1 Filter*

395 The transmittance curve and introduced polarization of the B1 filter are shown in Figures 27 and  
 396 28 respectively.

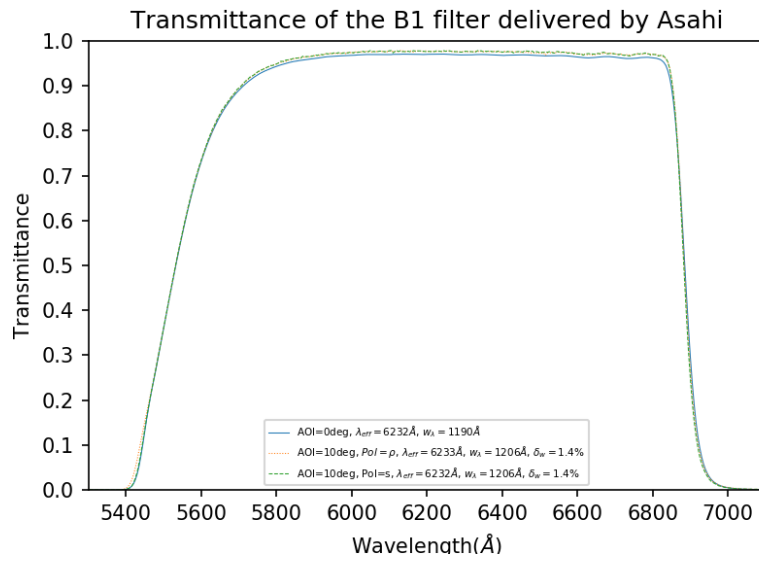


Fig 27: The transmittance curve of the B1 filter in different polarization states and 2 different angles of incidence.

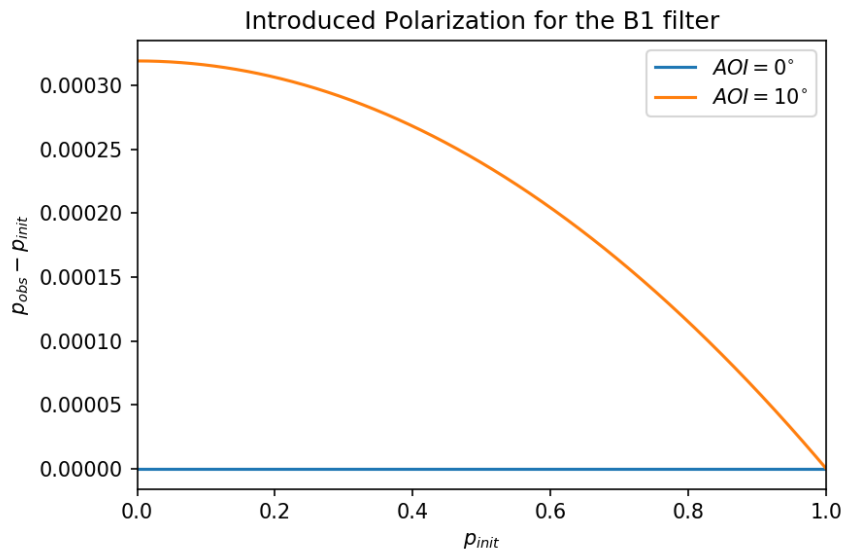


Fig 28: The polarization introduced by the B1 filter in 2 different angles of incidence (normal and extreme) as a function of the input polarization.

397 The 3-level interferometry and wavefront measurement of the B1 filter is shown in Figures 29,

398 30 and 31.

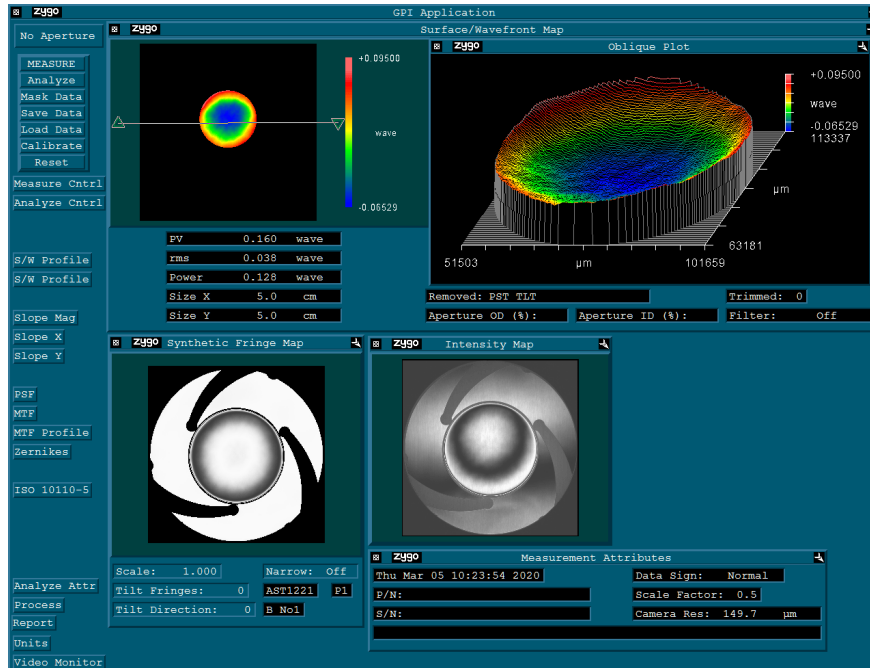


Fig 29: The first interferometric and wavefront measurement of the B1 filter.

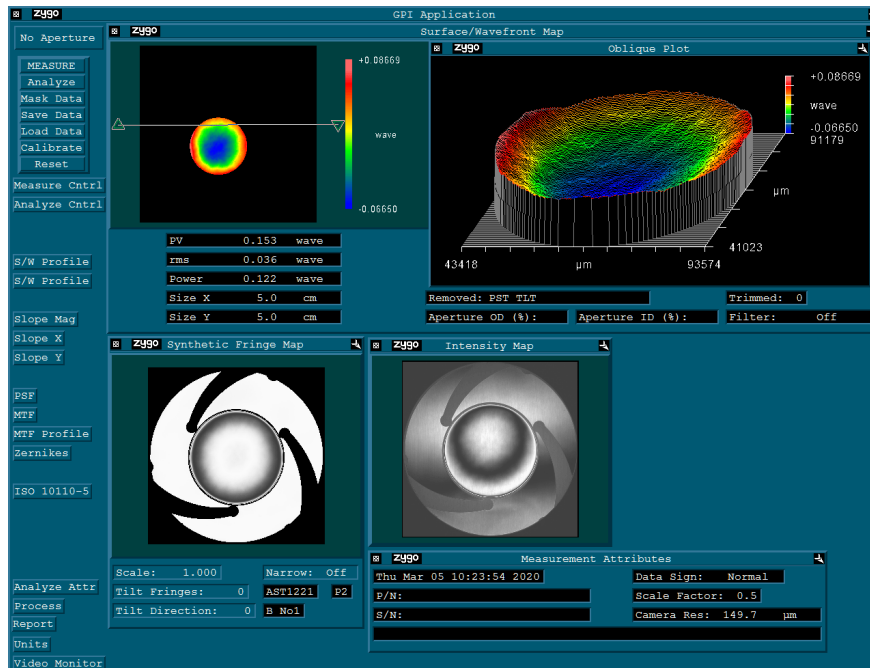


Fig 30: The second interferometric and wavefront measurement of the B1 filter.

399 *Disclosures*

400 The authors declare there are no financial interests, commercial affiliations, or other potential con-  
 401 flicts of interest that have influenced the objectivity of this research or the writing of this paper.

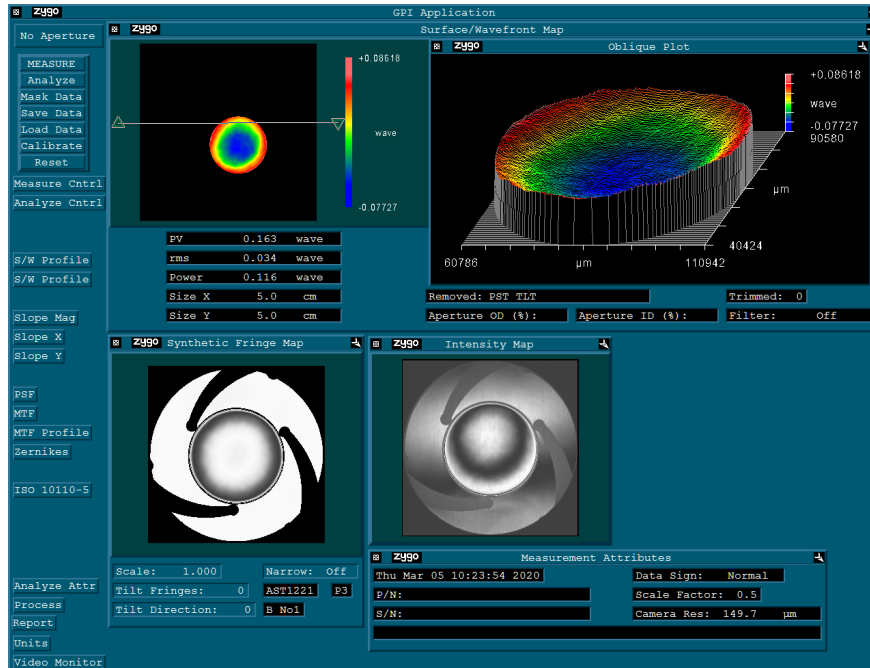


Fig 31: The third interferometric and wavefront measurement of the B1 filter.

402 *Code, Data, and Materials Availability*

403 The data and archived version of the code presented in this article are publicly available at the  
 404 GitHub repository: <https://github.com/HeisenbergK/NewWALOPCalibrate2Dens>.  
 405 [git](#).

406 *Acknowledgments*

407 The PASIPHAE program is supported by grants from the European Research Council (ERC) under  
 408 grant agreements No. 771282 and No. 772253; by the National Science Foundation (NSF) award  
 409 AST-2109127; by the National Research Foundation of South Africa under the National Equip-  
 410 ment Programme; by the Stavros Niarchos Foundation under grant PASIPHAE; and by the Infosys  
 411 Foundation.

412 VPa acknowledges support by the Hellenic Foundation for Research and Innovation (H.F.R.I.)

413 under the “First Call for H.F.R.I. Research Projects to support Faculty members and Researchers  
414 and the procurement of high-cost research equipment grant” (Project 1552 CIRCE).

415 VPa acknowledge support from the Foundation for Research and Technology - Hellas Synergy  
416 Grants Program through project MagMASim, jointly implemented by the Institute of Astrophysics  
417 and the Institute of Applied and Computational Mathematics.

418 KT and AP acknowledge support from the Foundation for Research and Technology - Hellas  
419 Synergy Grants Program through project POLAR, jointly implemented by the Institute of Astro-  
420 physics and the Institute of Computer Science.

421 TG is grateful to the Inter-University Centre for Astronomy and Astrophysics (IUCAA), Pune,  
422 India for providing the Associateship programme under which part of this work was carried out.

423 VPe acknowledges funding from a Marie Curie Action of the European Union (grant agreement  
424 No. 101107047).

#### 425 *References*

- 426 1 K. Tassis, A. N. Ramaprakash, A. C. S. Readhead, *et al.*, “PASIPHAЕ: A high-Galactic-  
427 latitude, high-accuracy optopolarimetric survey,” *arXiv e-prints* **0**, arXiv:1810.05652 (2018).
- 428 2 Pelgrims, V., Clark, S. E., Hensley, B. S., *et al.*, “Evidence for line-of-sight frequency decor-  
429 relation of polarized dust emission in planck data,” *A&A* **647**, A16 (2021).
- 430 3 V. Pelgrims, G. V. Panopoulou, K. Tassis, *et al.*, “Starlight-polarization-based tomography of  
431 the magnetized ism: Pasiphae’s line-of-sight inversion method,” (2022).
- 432 4 S. Maharana, J. A. Kyriotakis, A. N. Ramaprakash, *et al.*, “WALOP-South: A wide-field  
433 one-shot linear optical polarimeter for PASIPHAЕ survey,” in *Ground-based and Airborne*

- 434 *Instrumentation for Astronomy VIII*, C. J. Evans, J. J. Bryant, and K. Motohara, Eds., *Inter-*  
435 *national Society for Optics and Photonics* **11447**, 1135 – 1146, SPIE (2020).
- 436 5 S. Maharana, J. A. Kypriotakis, A. N. Ramaprakash, *et al.*, “WALOP-South: a four-camera  
437 one-shot imaging polarimeter for PASIPHAE survey. Paper I—optical design,” *Journal of*  
438 *Astronomical Telescopes, Instruments, and Systems* **7**, 014004 (2021).
- 439 6 S. Maharana, R. M. Anche, A. N. Ramaprakash, *et al.*, “Walop-south: A four-camera one-  
440 shot imaging polarimeter for pasiphae survey. paper ii – polarimetric modelling and calibra-  
441 tion,” (2022).
- 442 7 J. F. C. Wardle and P. P. Kronberg, “The linear polarization of quasi-stellar radio sources at  
443 3.71 and 11.1 centimeters.,” *ApJ* **194**, 249 (1974).
- 444 8 J. F. L. Simmons and B. G. Stewart, “Point and interval estimation of the true unbiased  
445 degree of linear polarization in the presence of low signal-to-noise ratios,” *A&A* **142**, 100–  
446 106 (1985).
- 447 9 P. Reig and E. Palaiologou, “Observing conditions at Skinakas Observatory,” *FORTH-IA* **0**  
448 (2020).
- 449 10 H. Nyquist, “Certain topics in telegraph transmission theory,” *Transactions of the American*  
450 *Institute of Electrical Engineers* **47**(2), 617–644 (1928).
- 451 11 C. Shannon, “Communication in the presence of noise,” *Proceedings of the IRE* **37**(1), 10–21  
452 (1949).
- 453 12 A. N. Ramaprakash, C. V. Rajarshi, H. K. Das, *et al.*, “RoboPol: a four-channel optical  
454 imaging polarimeter,” *MNRAS* **485**, 2355–2366 (2019).

- 455 13 J. Bailey, D. V. Cotton, L. Kedziora-Chudczer, *et al.*, “Hippi-2: A versatile high-precision  
456 polarimeter,” *Publications of the Astronomical Society of Australia* **37**, e004 (2020).
- 457 14 V. Piirola, A. Berdyugin, and S. Berdyugina, “DIPOL-2: a double image high precision  
458 polarimeter,” in *Ground-based and Airborne Instrumentation for Astronomy V*, S. K. Ram-  
459 say, I. S. McLean, and H. Takami, Eds., *Society of Photo-Optical Instrumentation Engineers*  
460 *(SPIE) Conference Series* **9147**, 91478I (2014).
- 461 15 D. Brewster, “IX. on the laws which regulate the polarisation of light by reflexion from trans-  
462 parent bodies. by david brewster, LL. d. f. r. s. edin. and f. s. a. edin. in a letter addressed  
463 to right hon. sir joseph banks, bart. k. b. p. r. S,” *Philos. Trans. R. Soc. Lond.* **105**, 125–159  
464 (1815).
- 465 16 O. G. King, D. Blinov, A. N. Ramaprakash, *et al.*, “The RoboPol pipeline and control sys-  
466 tem,” *MNRAS* **442**, 1706–1717 (2014).
- 467 17 Robin, A. C., Reylé, C., Derrière, S., *et al.*, “A synthetic view on structure and evolution of  
468 the milky way,” *A&A* **416**(1), 157 (2004).
- 469 18 “Asahi spectra.” <https://asahi-spectra.co.jp/>. Accessed: 2023-10-01.
- 470 19 R. M. Anche, S. Maharana, A. N. Ramaprakash, *et al.*, “Stress-induced birefringence in the  
471 lenses of Wide-Area Linear Optical Polarimeter-South,” in *Advances in Optical and Mechan-*  
472 *ical Technologies for Telescopes and Instrumentation, Society of Photo-Optical Instrumenta-*  
473 *tion Engineers (SPIE) Conference Series* **12188**, 121882C (2022).
- 474 20 P. Soleillet, “Sur les paramètres caractérisant la polarisation partielle de la lumière dans les  
475 phénomènes de fluorescence,” *Ann. Phys. (Paris)* **10**(12), 23–97 (1929).



- 476 21 K. Levenberg, “A method for the solution of certain non-linear problems in least squares,”  
477 *Quart. Appl. Math.* **2**(2), 164–168 (1944).
- 478 22 D. W. Marquardt, “An algorithm for least-squares estimation of nonlinear parameters,” *J. Soc.*  
479 *Ind. Appl. Math.* **11**, 431–441 (1963).
- 480 23 P. Virtanen, R. Gommers, T. E. Oliphant, *et al.*, “SciPy 1.0: Fundamental Algorithms for  
481 Scientific Computing in Python,” *Nature Methods* **17**, 261–272 (2020).
- 482 24 D. Blinov, S. Maharana, F. Bouzelou, *et al.*, “The robopol sample of optical polarimetric  
483 standards,” *A&A* **677**, A144 (2023).
- 484 25 S. Maharana, S. Kiehlmann, D. Blinov, *et al.*, “Bright-Moon sky as a wide-field linear Po-  
485 larimetric flat source for calibration,” *A&A* **679**, A68 (2023).
- 486 26 D. Malacara, M. V. Mantravadi, S. Mallick, *et al.*, *Optical shop testing*, Wiley Series in Pure  
487 and Applied Optics (1978).

488 **John Andrew Kypriotakis** is a Ph.D. student at the University of Crete, Greece, Department  
489 of Physics and at the Institute for Astrophysics of the Foundation for Research and Technology  
490 Hellas, Greece. He received his B.Sc. in Physics from University of Crete, Greece in 2017. He is  
491 currently working on the design and development of the WALOP instruments for the PASIPHAE  
492 survey. His areas of interest are Instrumentation (incl. Software), Data Analysis and Machine  
493 Learning.

494 **Siddharth Maharana** is a post-doctoral researcher at the South African Astronomical Observa-  
495 tory. He received his Bachelor in Mechanical Engineering from Central University, Bilaspur, India  
496 in 2015 and his PhD in Astronomical Instrumentation in the Inter University Centre for Astronomy

497 and Astrophysics, Pune India. He is currently working on the WALOP instruments for PASIPHAE  
498 survey. His areas of interest are polarimetric instrumentation and data analysis.

499 Biographies and photographs of the other authors are not available.

## 500 **List of Figures**

501 **1** The clearance inside the fork of the Skinakas observatory's 1.3m telescope. All  
502 measurements are in mm. FP is the used telescope's focal plane, after the shift  
503 described in Section 3.1.

504 **2** A conceptual diagram of the WALOP instruments. Light enters the collimator  
505 ("Col" - from the left, coming from the telescope). It is then fed to the polariza-  
506 tion array ("PA" - containing 2 Wollaston prisms side-by-side each preceded by  
507 a HWP), whereby is split into 4 beams. The now polarized light is focused by  
508 4 camera lens arrays ("Cam1-4") onto 4 separate CCDs. The diagram represents  
509 the WALOP-North instrument whose collimator receives unfocused light (as dis-  
510 cussed in Section 3), while WALOP-South receives the light already focused by  
511 the telescope. The arrows denote the polarization of the rays.

- 512 3 The shaded model of the instrument. Light coming from above passes through  
513 the collimator, enters the side-by-side Wollaston prisms (being split in 4 beams by  
514 polarization) and is re-directed horizontally to 4 separate camera arms. In each of  
515 those arms, a second fold redirects the light upwards towards a CCD. The linear  
516 polarizer is removable and rotatable, to be used for calibration (Section 6). As-  
517 terisks denote aspheric lenses. FP is the focal plane of the telescope (without the  
518 instrument optics) in the modified configuration of Section 3.1.
- 519 4 Comparison of a trailing guider concept, used in WALOP-South (left) and a rotat-  
520 ing guider concept, used in WALOP-North (right). The small squares in each case  
521 are the guider fields and the big ones, the science fields in each case (the rotating  
522 design's path has been truncated to  $90^\circ$  for illustration purposes).
- 523 5 Plot of the PSF along the x-axis (in  $\mu m$ ,  $px$ , and  $arcsec$ ) for each instrument de-  
524 tector. Each PSF is weight-averaged for wavelength (using the SDSS-r bandpass)  
525 and averaged for the entire FoV. Seeing is not included in this calculation.
- 526 6 Plot of the PSF along the x-axis (in  $\mu m$ ,  $px$ , and  $arcsec$ ) for each instrument de-  
527 tector. Each PSF is weight-averaged for wavelength (using the SDSS-r bandpass)  
528 and averaged for the entire FoV. Seeing is included in this calculation, by means of  
529 convolving the seeing-ignorant PSF of Figure 5 with a Gaussian kernel of FWHM  
530 equal to the mean seeing FWHM at Skinakas.
- 531 7 Encircled energy profiles for each detector and field position.
- 532 8 Spot diagram for the WALOP-North instrument. For every detector (columns)  
533 and field point (rows), the spot produced from 10000 simulated rays is depicted.  
534 Additionally, the RMS and Geometric radius (GEO) is mentioned next to the spot.

- 535 9 The polarization introduced by the conventional SDSS-r filter in different AOI as a  
536 function of the input polarization.  $p_{init}$  is the incident polarization to the filter and  
537  $p_{obs}$  is the observed polarization after the filter (by an ideal polarimeter).
- 538 10 The transmittance curve of the new non-polarizing SDSS-r filter in two perpendic-  
539 ular polarization states ( $\rho$  and  $s$ ) and angles of incidence (lines intentionally thin to  
540 help distinguish the graphs).  $\lambda_{eff}$  is the effective wavelength of the filter,  $w_\lambda$  is the  
541 filter wavelength-width, and  $\delta_w$  is the wavelength-width difference between each  
542 respective AOI and  $AOI = 0^\circ$ . Note: we chose the nomenclature "ρ" and "s" for  
543 the filter's perpendicular polarization states instead of the conventional "o" and "e"  
544 to reflect the difference of reference frame between the filter and Wollaston prism  
545 (since both these components have a separate polarization angle reference frame).  
546 The reference frame of the Wollaston prism corresponds with the EVPA reference  
547 frame.
- 548 11 The polarization introduced by the new non-polarizing SDSS-r filter in different  
549 angles of incidence as a function of the input polarization.
- 550 12 The FoV sampling we input to Zemax. (units of field are degrees)
- 551 13 The polarization sampling we input to Zemax.
- 552 14 Maps of the elements of the covariance matrix from the fit on Equations 3 and 4.
- 553 15 Maps of the standard deviations of the difference between the input and the re-  
554 trieved  $q$  and  $u$  ( $a$  and  $b$  respectively) from the calibration model. The closer to 0,  
555 the better.

- 556 16 Maps of the retrieved parameters for the 4 polar fully polarized input parameters.  
557 Maps (a) and (d) depict the throughput of the instrument, while (b) and (c) the  
558 cross-talk.
- 559 17 The transmittance curve of the A1 filter in different polarization states and 2 dif-  
560 ferent angles of incidence.
- 561 18 The polarization introduced by the A1 filter in 2 different angles of incidence (nor-  
562 mal and extreme) as a function of the input polarization.
- 563 19 The first interferometric and wavefront measurement of the A1 filter.
- 564 20 The second interferometric and wavefront measurement of the A1 filter.
- 565 21 The third interferometric and wavefront measurement of the A1 filter.
- 566 22 The transmittance curve of the A2 filter in different polarization states and 2 dif-  
567 ferent angles of incidence.
- 568 23 The polarization introduced by the A2 filter in 2 different angles of incidence (nor-  
569 mal and extreme) as a function of the input polarization.
- 570 24 The first interferometric and wavefront measurement of the A2 filter.
- 571 25 The second interferometric and wavefront measurement of the A2 filter.
- 572 26 The third interferometric and wavefront measurement of the A2 filter.
- 573 27 The transmittance curve of the B1 filter in different polarization states and 2 differ-  
574 ent angles of incidence.
- 575 28 The polarization introduced by the B1 filter in 2 different angles of incidence (nor-  
576 mal and extreme) as a function of the input polarization.
- 577 29 The first interferometric and wavefront measurement of the B1 filter.
- 578 30 The second interferometric and wavefront measurement of the B1 filter.

579 31 The third interferometric and wavefront measurement of the B1 filter.

## 580 **List of Tables**

581 1 Technical specifications for the WALOP-North Instrument.

582 2 Telescope and Site Details for the Skinakas 1.3m telescope.

583 3 Aspherical Lenses used in WALOP-North. ROC is the radius of curvature, D is the  
584 lens diameter, t is the thickness, and k is the conic parameter

585 4 Tolerancing parameters for the WALOP-North instrument.

586 5 Results of the Monte Carlo tolerance analysis for the WALOP-North instrument.

587 The criterion used was the RMS spot size. The maximum compensation of the  
588 back focus was  $1mm$ .

589 6 Photometric Calculations for the WALOP candidate filters.

590 7 Interferometric and spectroscopic performance of the manufactured WALOP fil-  
591 ters.